An ASTSEKF optimizer with nonlinear condition adaptability for accurate SOC estimation of lithium-ion batteries.

TAKYI-ANINAKWA, P., WANG, S., ZHANG, H., LI, H., YANG, X. and FERNANDEZ, C.

2023

An ASTSEKF optimizer with nonlinear condition adaptability for accurate SOC estimation of lithium-ion batteries

Paul Takyi-Aninakwa [a,*], Shunli Wang [a], Hongying Zhang [a], Huan Li [a], Xiao Yang [a], Carlos Fernandez [b]

[a] *School of Information Engineering, Southwest University of Science and Technology, Mianyang 621010, China*
[b] *School of Pharmacy and Life Sciences, Robert Gordon University, Aberdeen AB10-5GJ, UK*

* Corresponding author.:- e*mail address:* tapaul@mails.swust.edu.cn (P. Takyi-Aninakwa).

A B S T R A C T

Safe and reliable operations of lithium-ion batteries in electric vehicles (EVs), etc., highly depend on the accurate state of charge (SOC) estimated by the battery management system (BMS). However, due to the battery's nonlinear operating conditions and complex electrochemistry, accurately estimating SOC is a major challenge. In this paper, an adaptive strong tracking square-root extended Kalman filter (ASTSEKF) with nonlinear condition adaptability is proposed for the recursive correction, denoising, and optimization of the SOC estimation of lithium-ion batteries. The proposed ASTSEKF optimizer introduces an adaptive fading factor, a weight adjustor, and a strong tracking filter to recursively update the posteriori error covariance matrix using a Cholesky decomposition and corrects the uncertainties of the EKF method. The effectiveness of the ASTSEKF method is demonstrated by utilizing it to refine and enhance the estimations of a closed-loop nonlinear autoregressive model with exogenous input (NARX) and a deep feed-forward neural network (DFFNN) utilizing deep transfer learning techniques. The Levenberg-Marquardt and adaptive moment estimation approaches are employed to address gradient issues and stabilize the networks. Battery tests are carried out at different charge-discharge rates, temperatures, complex working conditions, and aging levels. The comparative SOC results show that the proposed ASTSEKF optimizer ensures an overall maximum mean absolute error, mean square error, and root mean square error improvements of 89.82%, 91.67%, and 90.76%, respectively. Additionally, it denoises, stabilizes, optimizes, and quickly converges the final SOC with a good balance between optimal accuracy and computational complexity. In comparison to other existing methods, the proposed ASTSEKF optimizer can overcome nonlinearities encountered by the BMS under various operating conditions to provide accurate SOC estimation in EVs.

Keywords:
State of charge; Lithium-ion battery; Nonlinear autoregressive model with exogenous input; Adaptive strong tracking square-root extended Kalman filter; Deep feed-forward neural network

Nomenclature

Abbreviations and acronyms	
ADAM	Adaptive moment estimation
ASTSEKF	Adaptive strong tracking square-root extended Kalman filter
BBDST	Beijing bus dynamic stress test
BMS	Battery management system
CC-CV	Constant current-constant voltage
DFFNN	Deep feed-forward neural network
DL	Deep learning
DTL	Deep transfer learning
DST	Dynamic stress test
EV	Electric vehicle
HPPC	Hybrid pulse power characterization
LM	Levenberg-Marquardt
Li-NCM	Lithium nickel cobalt manganese
Li-NCA	Lithium nickel cobalt aluminum
MAE	Mean absolute error
ME	Maximum error
NARX	Nonlinear autoregressive model with exogenous input
RMSE	Root mean squared error
RT	Room temperature
SOC	State of charge
SOH	State of health
c	Distribution factor
d_x	Input delay coefficient
d_y	Output delay coefficient
x_{max}	Maximum data value
z	Distribution matrix

x	Original data
$\widehat{x}$	State estimate
S	Upper triangular matrix
P	Posteriori error matrix
K	Kalman gain
q	Uncertainty parameter
f	Nonlinear function
Q	Process noise
R	Measurement noise
e	Innovation residual
g	Forgetting factor
d	Weighing coefficient
α	Adaptive fading factor
γ	Adaptive weighing factor
A	State transition matrix
B	Control input matrix
C	Measurement matrix
I	Identity matrix
k	Time step
Q_n	Nominal capacity
η	Coulombic efficiency
λ	Strong tracking filter
y	Actual SOC value
$\widehat{y}$	Estimated SOC value
E	Estimated SOC error value
N	Total number of data samples
x_n	Normalized data value
x_{min}	Minimum data value

1. Introduction

Because of the need for a green environment, battery technology is gaining traction for applications in portable electronic gadgets, electric vehicles (EVs), sustainable energy systems, etc. Lithium-ion batteries are preferred in these applications due to their appreciable advantages, such as high specific energy, high power density, high voltage, more usable capacity, no memory effect, low self-discharge rate, longevity, etc. [1,2]. The ability to store energy and provide optimal power decreases with the loss of active materials and lithium-ion inventory, which nonlinearly reflects the decrease in capacity and increase in the internal impedance of the battery [3–5]. Several known problems, such as undetectable performance deterioration, accelerated aging, explosions, etc., have been encountered with lithium-ion batteries due to inaccurate estimation of crucial state parameters [6,7].

The battery management system (BMS) is an embedded electronic module that holds the key to efficient and reliable system operation by monitoring the working states, such as operating temperatures, charge-discharge rates, battery aging, etc., as well as the users' safety in practical applications [8,9]. It also keeps the battery in a condition that allows it to fulfill its functional design requirements and make the best use of it [10]. Among several functions, the embedded BMS in EVs ensures accurate estimation of the battery's state parameters, including the state of charge (SOC), state of health (SOH), etc. The SOC is defined as the ratio of the remaining capacity to the nominal capacity of the battery, which is usually expressed as a percentage (0–100%). Accurately estimating the SOC not only indicates how much capacity is available but also helps users avoid unexpected system interruptions, determine the remaining drive range in EVs, prevent over-charge and over-discharge of the battery, etc. [11]. However, due to the high nonlinearities caused by the battery materials and the dynamic operating conditions, it cannot be measured directly, but its value can be estimated using quantifiable battery parameters, such as current, voltage, and temperature [12].

1.1. SOC estimation method classifications

Over the years, numerous SOC estimation methods have been proposed for the BMS. Collectively, these methods can be divided into four categories: direct measurement, ampere-hour (Ah) integral, battery model-based, and data-driven methods [13–15]. The direct measurement methods are based on battery parameter characterization, which includes electrochemical impedance spectroscopy (EIS), open-circuit voltage (OCV) methods, internal resistance method, etc. [16,17]. The EIS evaluates the impedance properties of the battery across a broad frequency range. Although it has a simple implementation, its computation is sophisticated, with high sensitivity to the battery's status and environmental conditions [18,19]. On the other hand, the OCV method estimates the SOC of the battery based on the OCV-SOC relationship. However, when the battery's OCV-SOC relationship and measurement voltage are inaccurately modeled, it results in inaccurate SOC estimation. Therefore, it necessitates a long resting time to recover and measure the OCV value accurately, making them impractical for onboard BMS applications [20,21]. The Ah integral method is experimentally conducted by integrating the current flowing to and from the battery. This method is simple and easy to construct and implement on the BMS [22]. However, it solely depends on the initial SOC value, which can only be determined by the precise measurement of the load current, which is difficult to achieve in real-time. The battery model-based methods regard the SOC as a hidden state and constructs a state-space equation that has a relationship with the SOC using measured variables like the working current and voltage. A battery model, mostly an equivalent circuit model (ECM), is established for the state observer to characterize the dynamic parameters, which largely determine the accuracy [23,24]. For instance, an SOC and SOH co-estimation-based dual fractional-order extended Kalman filter is proposed based on the fractional-order ECM, whose parameters are identified using a hybrid genetic algorithm-particle swarm optimization by considering various driving cycle tests [25]. However, for this method, when the battery is subjected to a complex load profile and adverse working conditions, the voltage characteristics become extremely difficult to factor into the design of the ECM established for the state observer, resulting in laborious trial-and-error parameter identification processes and inaccurate SOC estimation [26–28].

Due to technological advancement, data-driven methods have been significantly utilized because of their excellent self-adaptation, self- learning, and high estimation accuracy of the state parameter [29]. It regards the battery as a "black box" rather than a practical mathematical estimation model. Through the utilization of feature extraction and a sufficient amount of training data, it directly maps the nonlinear relationship, which reflects the characteristic voltage responses of the battery [30,31]. These methods have served as the most favorable method to overcome the limitations of other existing methods [32]. Because of their simple architecture and efficient computation, deep learning (DL) methods such as deep feed-forward neural network (DFFNN), convolutional neural network (CNN), long short-term memory (LSTM) network, gated recurrent unit (GRU) network, nonlinear autoregressive model with exogenous input (NARX), etc., have been proposed for SOC estimation [33]. These methods can self-learn their weights and biases using gradient descent methods without any mathematical models. Furthermore, they accurately estimate SOC with a single set of model parameters, whereas other conventional methods require multiple models with varying parameters under different working states [34,35].

1.2. Literature review

Several DL-based models have been proposed for SOC estimation of lithium-ion batteries considering different working profiles and conditions. Fan et al. [36] proposed a CNN with a U-net architecture to address the boundary effect of the convolutional layer and improve the accuracy of the estimation at temperatures of 0 and 25 °C using a 2.9 Ah Panasonic 18650PF Li-NMC battery. Chen et al. [37] established a GRU network and proposed a genetic algorithm (GA) to optimize the key parameters of the network using a 2.5 Ah Sony US18650VTC5A battery for SOC estimation at temperatures of 0–45 °C. Yang et al. [38] established a GRU-RNN to estimate SOC at temperatures ranging from 10 to 50 °C using a 1.3 Ah BAKB18650CD Li-NMC battery. Tian et al. [39] proposed an LSTM network to estimate the SOC with an ACKF method for optimization under two working conditions at temperatures ranging from 10 to 50 °C using a 2.23 Ah 18650 LiFePO$_4$ battery. Bian et al. [40] proposed a computationally complex stacked bidirectional LSTM network for SOC estimation at 0, 10, and 25 °C under two working conditions using 2.9 Ah Panasonic NCR18650PF and 2.0 Ah INR18650-20R lithium-ion batteries. Using the NARX network, Wang et al. [41] proposed a NARX network for SOC estimation of lithium-ion batteries with a moving window method that prevents the vanishing and explosion of the gradient at temperatures of 0, 25, and 45 °C and two working conditions using a 2.4 Ah NCR18650PF battery. Herle et al. [42] established a NARX network for SOC estimation at room temperature (RT) conditions and verified it under four working conditions using different hyperparameters using a 2.9 Ah Panasonic 18650PF battery with Li-NCA chemistry. Lipu et al. [43] proposed a NARX network and used a lighting search algorithm to find the best value of input delays, feedback delays, and hidden layer neurons for SOC estimation under two working conditions at temperatures of 0, 25, and 45 °C using a 2.0 Ah 18650 Li-NMC battery. Sun et al. [44] conducted a comparative study of a NARX and a radial basis function by optimizing both with the

UKF method under different hyperparameter selections using a 3.45 Ah Sanyo NCR 18650G lithium-ion battery. Guo et al. [45] established a NARX network and used a GA to improve the accuracy of the estimated SOC using a 2.0 Ah NASA battery, #6. Abbas et al. [46] studied the performance comparison of NARX and LSTM networks for SOC estimation at a temperature range of 5 to 25 °C using a 1.1 Ah LiFePO$_4$ battery. Wei et al. [47] proposed a hybrid NARX-LSTM model for SOC estimation and compared it to other established models at RT conditions under two working conditions using a 1.1 Ah 18650 LiFePO$_4$ battery. The aging process of a battery is affected by external factors such as complex temperatures and working conditions as well as internal degradation caused by side reactions. To address this, a data-based histogram framework that includes several methods is proposed for predicting battery aging trajectory and lifetime under various operating conditions. These methods include kernel-based, decision tree-based, probabilistic-based, and neural network-based methods [25]. The framework shows the significant impact that aging has on the battery.

However, because the SOC estimation process is affected by nonlinear factors such as temperature, charge-discharge rate, voltage characteristics, aging status, battery chemistry, etc., it is difficult to estimate accurately in real-time [48,49]. From the above studies, it can be observed that the conditions considered are mainly temperature variations ranging from 0 to 50 °C using batteries with small capacities (1.1–3.45 Ah) using DL-based networks. Also, the performance at different charge-discharge rates and aging levels is not considered to verify the robustness of their proposed SOC models [50]. Therefore, it is essential to model an advanced and robust SOC estimation method with optimized dynamic operating condition adaptability and high accuracy that is tested and verified using different operating conditions and battery status to ascertain the applicability of the proposed method for real- time BMS applications.

1.3. Contributions of this paper

In this paper, an adaptive strong tracking square-root extended Kalman filter (ASTSEKF) with an adaptive fading factor, a weight adjustor, and a strong tracking filter is proposed to recursively update and correct the Cholesky decomposition and uncertainties of the EKF method to denoise, stabilize, and optimize the final SOC of the NARX and DFFNN. The neural networks are established with a deep transfer learning (DTL) technique to enhance their generalizability and are optimized using Levenberg-Marquardt (LM) and adaptive moment estimation (ADAM) optimization methods to solve the gradient problems and stabilize the networks. The main contributions of the paper are highlighted below:

(1)   Using the LM and ADAM methods solves the gradient problems and enhances the hyperparameters, which improves the generalizability of the networks to estimate the SOC under various operating conditions and battery status.
(2)   The proposed ASTSEKF optimizer recursively updates the posteriori error covariance matrix using a Cholesky decomposition and corrects the uncertainties to ensure accurate SOC results under different operating conditions and battery status. It also can correct large initial SOC convergence and end-of-discharge errors. Furthermore, its formulation allows for a hybrid estimation framework, regardless of the working conditions.

1.4. Paper organization

The remaining sections of this paper are organized as follows: Section 2 introduces the modeling architecture of the SOC estimation methods. Section 3 describes the experimental platform, test procedures, and data characteristics. Section 4 contains the results, discussion, and evaluations of the proposed method. Finally, the conclusion and future work are presented in Section 5.

2. Modeling architecture of the SOC estimation methods

2.1. Schematic formulation of the NARX network

The DTL technique refers to a class of network architecture that aims at solving state estimation problems by improving the generalizability of neural networks [51]. NARX is an improvement and outperforms the linear autoregressive model with exogenous input and the conventional RNN in predicting nonlinear and time-series problems in terms of deep-learning ability, convergence speed, generalizability, and accuracy [43]. In this paper, the closed-loop architecture is used because, instead of fully utilizing hidden layers, it forms output layers using limited feed- back connection layers with online estimation ability to improve the network's convergence speed and accuracy, which makes it suitable for EV applications [42]. The functional equation of the NARX network, consisting of three layers, is presented in Eq. (1).

$$y(k) = f\left[y(k-1), y(k-2), ..., y(k-d_y), x(k), x(k-1), x(k-2), ..., x(k-d_x)\right] + e(k) \tag{1}$$

In Eq. (1), $x(\bullet)$ and $y(\bullet)$ represent the input and output of the network, respectively, at each discrete time step k. $f(\bullet)$ is the nonlinear activation function, d_x and d_y represent the time delays of the input and output coefficients, respectively. $e(k)$ is the network's error between the actual and estimated outputs and $(\bullet)$ is the multiplication operator. The model expression for multi-dimensional inputs and one-dimensional output of the network is presented in Eq. (2).

$$y(k) = f_o\left[b_o + \sum_{h=1}^{N} w_{h_o} \bullet f_h\left(b_h + \sum_{i_1=0}^{dx_1} w_{i_1|h}x_1(k-i_1)\right) + \sum_{i_2=0}^{dx_2} w_{i_2|h}x_2(k-i_2) + \sum_{i_3=0}^{dx_3} w_{i_3|h}x_3(k-i_3) + \sum_{j=0}^{d_y} w_{jh}y(k-j)\right] \tag{2}$$

In Eq. (2), $f_o(\bullet)$ and $f_h(\bullet)$ are the nonlinear activation functions of the output and hidden layers, respectively. i_k represents the input delay of the hidden layers. $w_{i1}|h$, $w_{i2}|h$, and $w_{i3}|h$ are the associated weights from the first, second, and third inputs to the respective hidden layers. b_o and bh are the biases of the output and hidden layers, respectively, added to strengthen and ensure the flexibility of the network.

For the hyperparameters, the training epoch, goal, and gradient values are set to 300, 10^{-10}, and 10^{-6}, respectively. The input delay, feedback delay, and hidden layer size are defined as 1:4, 1:4, and 10, respectively. Through iterative optimization, the ideal dropout rate in this paper is defined as 0.1 with a learning rate of 0.01 and a "trainlm" training function. The perceptron applies a tangent sigmoid transfer function (tansig) and a linear transfer function (purelin) to the hidden and output layers, respectively [52]. The typical architecture of the closed-loop NARX network is presented in Fig. 1.
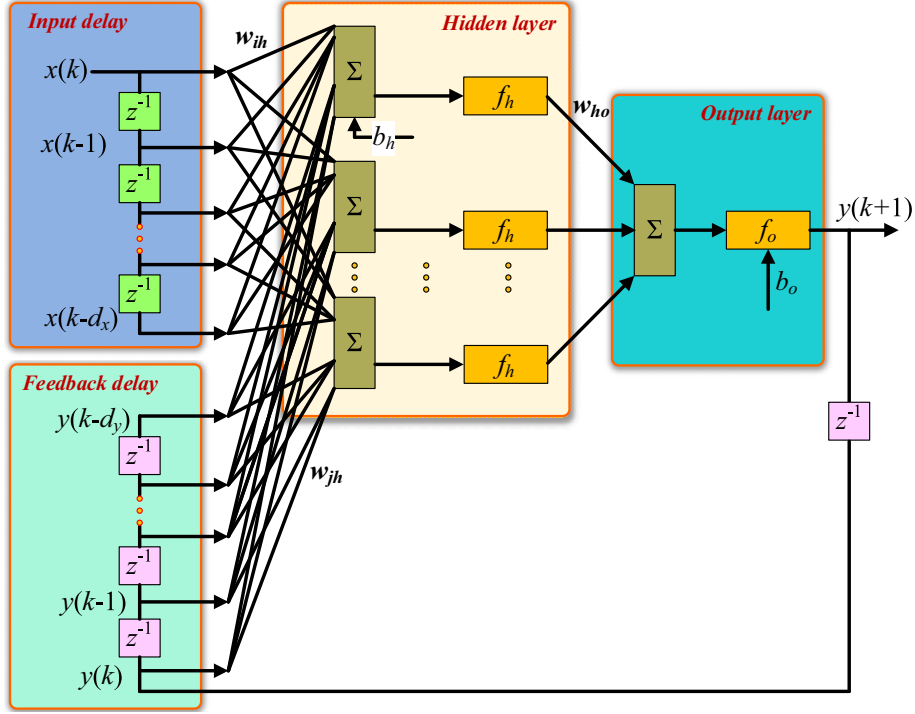
Fig. 1. Schematic representation of the closed-loop NARX network.

The DFFNN is established by constructively adding hidden layers to the conventional FFNN. As the distribution of the weights is determined by optimizing the training dataset might exhibit invariance for a large number of hidden neurons. The additional hidden layers will help minimize the error and improve the estimated SOC value of the battery. It provides advantages in machine learning by allowing data to be processed independently with several neurons to achieve accurate moderation in a short time.

The working mechanism of the DFFNN is unidirectional from the input to the output layer. The input, x_k, goes through a series of matrix multiplications to yield the output, y_k. The network's hidden layer activation, h is mathematically expressed in Eq. (3).

$$h_a^n = \sigma\left(\sum_k w_{j,k}^n h_k^{n-1} + b_k^n\right) \tag{3}$$

In Eq. (3), w^n is the weight, and b^n is the bias of the layer n. a^n is the activator of the layer n and σ is the rectified linear unit (ReLU) activation function. The network's output is mathematically expressed in Eq. (4).

$$\begin{cases} SOC_k = f\left(\sum_{k=1}^{N} x_{j,k} w_{j,k} h_{j,k} + b_{j,k}\right) \\ f(x) = \dfrac{1}{1+e^{-x}} \end{cases} \tag{4}$$

In Eq. (4), $x_{j,k}$ is the neuron input. $w_{j,k}$ and $b_{j,k}$ are the weight and bias, respectively, from the hidden layer to the hidden layer at time step k. $f(\bullet)$ is the nonlinear sigmoid activation function and N is the total number of samples. $h_{j,k}$ refers to the output of the hidden layer at time step k. Because the weight distribution is determined by optimization, the training dataset may show invariance for a large number of nodes. The overfitting of the DFFNN caused by too many hidden layers and of each hidden layer, improving training time, stability, and SOC estimation ability. Fig. 2 depicts the architecture of the established DFFNN.
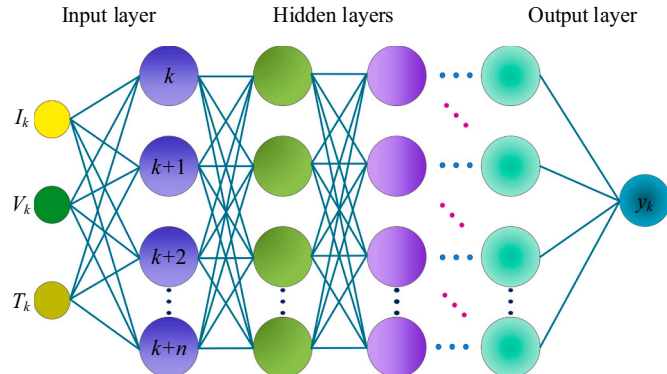

Fig. 2. Schematic representation of the established DFFNN.

There are several hyperparameter optimizations and tuning options available, allowing you to find the best combination for each specific time-series prediction. However, hyperparameter optimization is a relatively new field of study that is beyond the scope of this study. For this network, the hyperparameters selected for the training epoch, feedforward-net, hidden neuron, and batch size values of 300, 15, 64, and 32, respectively. The ReLU activation function is used for batch normalization with a learning rate of 0.01 and a "trainlm" training function.

2.3. Networks optimization and training

In this paper, the training and testing of the established networks for SOC estimation are conducted using MATLAB 2021 on a computer with an Intel(R) Core (TM) i5-7300HQ and a 2.50 GHz CPU. To solve the occurrence of the gradient explosion and vanishing problems, the LM method combines the gradient descent and Gauss-Newton methods by adaptively varying their updates [53]. By updating the parameters along the steepest-descent direction, the gradient descent method reduces the sum of the squared errors. By assuming that the least-squares function is locally quadratic in the parameters and locating the minimum of this quadratic, the total of the squared errors is decreased by the Gauss-Newton method [54]. The calculation employs the second derivative approach, which substantially prevents the networks from entering the local optimum [55]. The mathematical expression of the LM method for the adaptive update of the hyperparameters is shown in Eq. (5).

$$x_{k+1} = x_k + \left[J_k^T J_k + qD \right]^{-1} J_k^T e_k \tag{5}$$

In Eq. (5), x_{k+1} and x_k are the input vectors at the respective iteration time steps, and J_k is the Jacobian matrix including the first derivatives of the networks' errors with respect to the weights and biases. D is an identity matrix, e_k is the network's error, and   is an uncertainty parameter used to tune the computational accuracy and speed. The LM method offers good stability, quick convergence, and solves gradient problems.

For the training, an ADAM optimizer, which combines the adaptive gradient and root mean squared propagation is used [56]. It has the capability of calculating the adaptive learning rate for different parameters with fewer storage requirements and is applied in addition to the LM method to optimize the network's weights and biases based on the gradient of the objective function. Most frequently, a training epoch consists of one or more batches. Each batch is trained twice, once forward and once backward, giving each sample in the mini-batch a chance to adaptively update the internal networks' hyperparameters. Until a convergence condition is fulfilled, the forward and backward passes are continuously used to update the network weights and biases. The dropout technique is used between the network's hidden and fully connected layers. The main reason is to randomly set some neurons' output to zero while they are being trained. The dropout technology is not used during testing so that it will not have an impact on the output of neurons. After selecting the optimal hyperparameters and applying the LM and ADAM methods to optimize the input delays, feedback delays, and hidden neurons, the loss value for the objective function is expressed in Eq. (6).

$$Objective\ function = min \left[\frac{1}{N} \sum_{k=1}^{N} (y_k - \widehat{y}_k)^2 \right] \tag{6}$$

In Eq. (6), y_k is the estimated SOC value, y_k, is the actual SOC value, and N is the total number of observation data samples.

2.4. Data description and pre-processing

The data-driven networks are first trained on a specific type of dataset before being tested on previously unseen datasets to assess the generalizability and robustness of SOC estimation. Since data pre- processing is significant for accurate SOC estimation by the networks, the associated current, voltage, and temperature $[I_k, V_k, T_k]$ variables are measured based on the real-time operating conditions for the different charge-discharge rates and temperature studies while the SOC estimation at different SOH levels adds the capacity variables (Q_k).

Before training and testing, the datasets are normalized to improve robustness and convergence rate, as well as accelerate the gradient descent of the networks. The minimum-maximum normalization is adopted 4to map the measured battery data into the output range of [-1,1] using the expression in Eq. (7).

$$x_n = \frac{2(x - x_{min})}{x_{max} - x_{min}} - 1 \tag{7}$$

In Eq. (7), x is the original value. x_{min} and x_{max} are the minimum and maximum values in the datasets, respectively. x_n is the corresponding normalized value, which is the original input data of the networks.

The accuracy of SOC estimations is impacted by several complex working conditions and the loss of neighborhood information in the networks. Despite using the LM and ADAM methods to stabilize and solve gradient problems, the nonlinearities in battery operation result in suboptimal SOC accuracies. To address this, a new method called AST- SEKF is proposed and detailed in Section 2.5.

2.5. ASTSEKF-based optimization method

The EKF applies a partial derivative and first-order Taylor series expansion to the system's state-space equation, which results in high inaccuracies due to its inability to fully correct the uncertainties and noise. In this paper, a square-root decomposition and strong tracking filter are proposed for the posteriori error covariance matrix update of the EKF method. In the adaptive square-root extended Kalman filter, the posteriori error covariance matrix Pk of the EKF is decomposed as SkSTk for the iterative update. It ensures that the matrix assumes a symmetric form and a positive definite matrix in finite precision arithmetic to Cholesky decomposition. The Cholesky decomposition uses the square- root method for the posteriori error covariance matrix Pk, as expressed in Eq. (8).

$$P_k = S_k S_k^T \tag{8}$$

In Eq. (8), S_k is the upper triangular matrix. It also uses the Sage-Husa adaptive filter to update the noise variables and performs square-root decomposition on the posteriori error covariance matrix to ensure a positive definiteness matrix. Then, an adaptive strong tracking (AST) filter is added in addition to the adaptive fading and weight adjustment factors to make the residual error series orthogonal to each other. The working steps of the proposed ASTSEKF method are presented in Table 1.

Table 1
Working steps of the proposed ASTSEKF method.

Initialization of state variables	$\widehat{x}_0^+, P_0^+, Q_0, R_0$
Time update	
Priori state estimate	$\widehat{x}_{k\|k-1}^- = A_k \widehat{x}_{k-1\|k-1}^- + B_{k-1} u_{k-1}$
Priori error covariance matrix	$S_k^- = \begin{bmatrix} S_k^T A_k^T \\ \left((Q_k)^{1/2} \right)^T \end{bmatrix}^T$
Kalman gain	$\begin{cases} K_k = P_k^- F_k \left[F_k P_k^- F_k^T + R_k \right]^{-1} \\ \quad F_k = S_{k-1}^T C_k \end{cases}$
Measurement update	
Residual	$e_k = y_k - \widehat{y}_k$
Posteriori state estimate	$\widehat{x}_{k\|k} = \widehat{x}_{k\|k-1}^- + K_k e_k$
Posteriori error covariance matrix	$\begin{cases} S_k = S_k^- \left[I - \alpha_k \gamma_k \lambda_k F_k F_k^T \right] \\ \alpha_k = \dfrac{1 \pm \sqrt{\gamma_k z Q_k}}{1 - \sqrt{\gamma_k Q_k}} \\ \gamma_k = \left[F_k^T F_k + c R_k \right]^{-1} \end{cases}$
System and measurement noise matrix updates	$\begin{cases} Q_k = (1 - d_k) Q_{k-1} + d_{k-1} (K_k e_k K_k^T e_k^T + P_k \\ \qquad - A_k P_{k-1} A_k^T) \\ R_k = (1 - d_k) R_{k-1} + d_{k-1} \left(e_k e_k^T - C_k P_k^- C_k^T \right) \end{cases}$

A_k and B_k are the state-transition matrix and control-input matrix, which are applied to the state x_{k-1} and control-input vector u_k, respectively. C_k is the measurement matrix at time step k, which maps the state space into the measured space, which is initialized as 1. Since the error covariance matrix is decomposed, it can prevent the filter divergence caused by the filter's uncertainties, which is an assurance that P_k is always a positive definte matrix. I and e_k is the identity matrix and the residual, respectively.

In this paper, α is the adaptive fading factor used to suppress the noise by decreasing the value of the coefficient and vice versa, which is tuned within $0.8 < \alpha \leq 1$. γ is the weighing factor used to correct the fluctuation and stabilize the estimated SOC, whose values are set as $\gamma = 1, 2$, and 3 depending on the estimation accuracy. c is the distribution factor, which is used to incorporate the prior knowledge of the Gaussian distribution by tuning it as $0 \leq c \geq 1$. Then, λ is the strong tracking filter used to consistently update and correct the posteriori error covariance matrix. Its calculation is expressed as presented in Eq. (9).

$$\lambda_k = \begin{cases} \lambda_0, \lambda_0 > 1 \\ 1, \lambda_0 \leq 1 \end{cases}$$

$$\lambda_0 = \frac{\operatorname{tr}[M_{k+1}]}{\operatorname{tr}[N_{k+1}]}$$

$$\begin{cases} M_k = V_k - F_{k-1} F_{k-1}^T Q_{k-1} - \beta R_{k-1} \\ N_k = A_{k-1} F_k F_k^T P_{k\|k-1} A_{k-1}^T \end{cases} \tag{9}$$

$$V_{k+1} = E\{z_k z_k^T\} = \begin{cases} z_1 z_1^T, k = 0 \\ \dfrac{\rho V_k + z_{k+1} z_{k+1}^T}{1 + \rho}, k \geq 1 \end{cases}$$

In Eq. (9), V_k is the residual covariance matrix, and z is the distribution matrix. $0 < \rho \leq 1$ is the strong tracking-forgetting factor. $\beta \leq 1$ as a weakening factor is adjusted based on the degree of the mismatch and the current outcome of the estimation. Both the strong tracking-forgetting and weakening factors are intuitively adjusted based on estimation accuracy.

The Sage-Husa method compares the final estimated value to the initial estimated value to update the noise variables. To make the estimation of noise more accurate and avoid the influence of the measured value, this paper considers the noise at the previous and current time steps to adopt a weighing coefficient d_k, as presented in Eq. (10).

$$d_k = \frac{1 - g}{1 - g^{N+1}}, N = 0, 1, 2, \ldots, n \tag{10}$$

In Eq. (10), N and n are the individual time step and last sample numbers, respectively. Meanwhile, because the value of the forgetting factor g represents the relative weight of the old and new data, as the model error increases, the weight of the new data should increase, resulting in a decrease in the forgetting factor value, and vice versa. To maintain a good balance between tracking ability and computational efficiency during the noise updates, reduce the influence of historical information, and emphasize new information, the range of the forgetting factor is tuned between $0.95 \leq g \geq 1$. It thus resolves the problem of data saturation and improves the method's anti-interference capabilities.

The ratio of the remaining useful capacity to the nominal capacity of the battery is characterized as the SOC. Its mathematical calculation is expressed in Eq. (11).

$$SOC_k = SOC_0 - \frac{1}{Q_n} \int_0^N \eta I_{L,k} dk \tag{11}$$

In Eq. (11), SOC_k is the current SOC estimated value at time step k, SOC_0 is the initial SOC value at the initial time step, and N is the total number of samples. ŋ is the Coulombic efficiency, which is defined as 1. $I_{L,k}$ is the working current time at step k, and Q_n is the nominal capacity of the battery.

2.6. Schematic framework of the hybrid models

The entire estimation framework, including the selected battery test conditions and profiles, data pre-processing, etc., in addition to the verification and comparative studies of the performance of the proposed ASTSEKF optimizer, are presented in Fig 3.
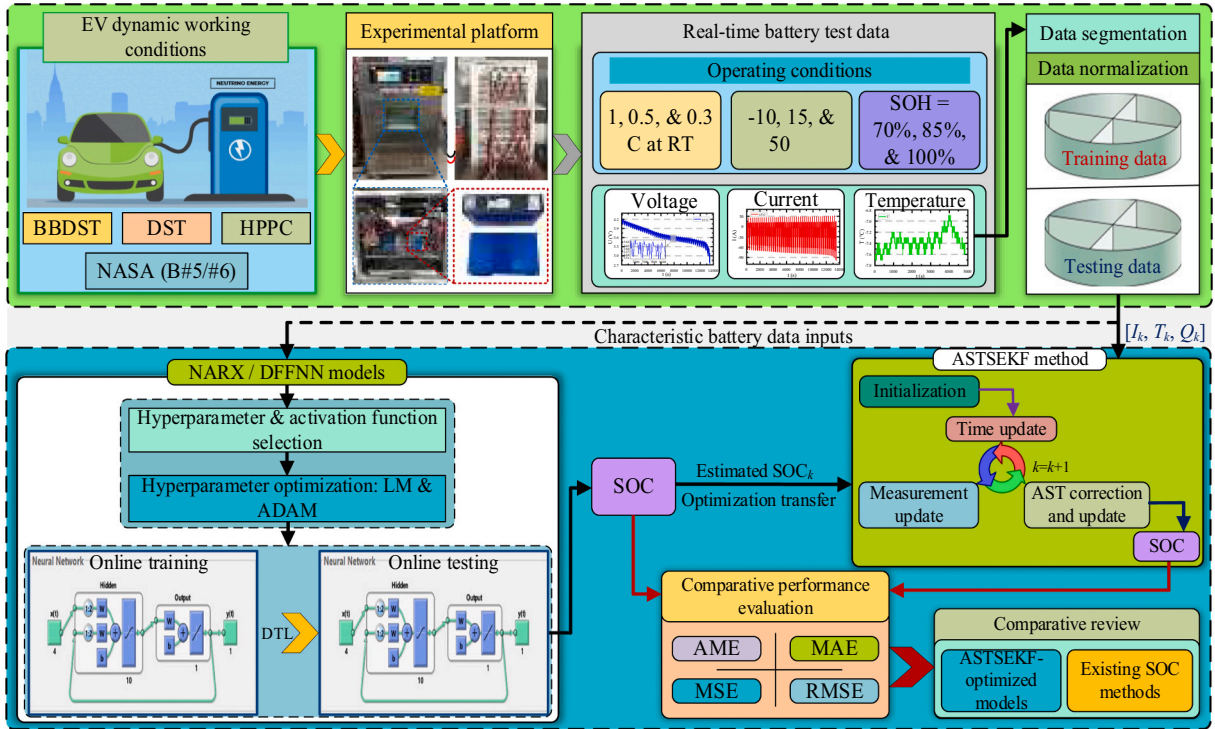

Fig. 3. Schematic framework of the NARX/DFFNN-ASTSEKF models for SOC estimation.

Fig. 3 shows that the input variables transferred for the optimization by the ASTSEKF method are the estimated SOC by the networks, the corresponding current (I_k), temperature (T_k), and capacity (Q_k) variables for denoising, stabilizing, and optimizing the final SOC. Then, comparative performance evaluations of the NARX and DFFNN with their ASTSEKF-based optimized variants are conducted using the absolute maximum error (AME), mean absolute error (MAE), mean square error (MSE), and root mean square error (RMSE) metrics. Finally, superiority analyses are conducted for the proposed models and other existing SOC estimation methods using their optimal values to verify the performance of the ASTSEKF method.

2.7. Method verification criteria

In this paper, to critically verify the performance of the networks and the proposed ASTSEKF-based optimization method for SOC estimation, the AME, MAE, MSE, and RMSE metrics are employed. Their mathematical calculations are expressed in Eq. (12).

$$\begin{cases} E_k = y_k - \hat{y}_k \\ AME = max_k 1, 2, ..., N|E_k| \\ MAE = \frac{1}{N} \sum_{k=1}^{N} |E_k| \\ MSE = \frac{1}{N} \sum_{k=1}^{N} (E_k)^2 \\ RMSE = \sqrt{\frac{1}{N} \sum_{k=1}^{N} (E_k)^2} \end{cases} \tag{12}$$

In Eq. (12), k is the non-missing data time step, N is the total number of data samples, and E_k is the estimated SOC error value at time step k. y_k is the estimated SOC error value at time step k. y_k is the actual SOC value and $\hat{y}_k$ is the estimated SOC value by the proposed methods at the time step k.

3. Experimental platform and data characteristics

Two battery chemistries, Li-NCM and Li-NCA, are used for this study. For the different charge-discharge rate and temperature tests, the Li-NCM70Ah battery is used as the research object. Meanwhile, for the aging tests, Li-NCA1.86/2.04 Ah batteries are used as the research object. The basic technical specifications of the batteries are presented in Table 2.

Table 2
Basic technical specifications of the lithium-ion batteries.

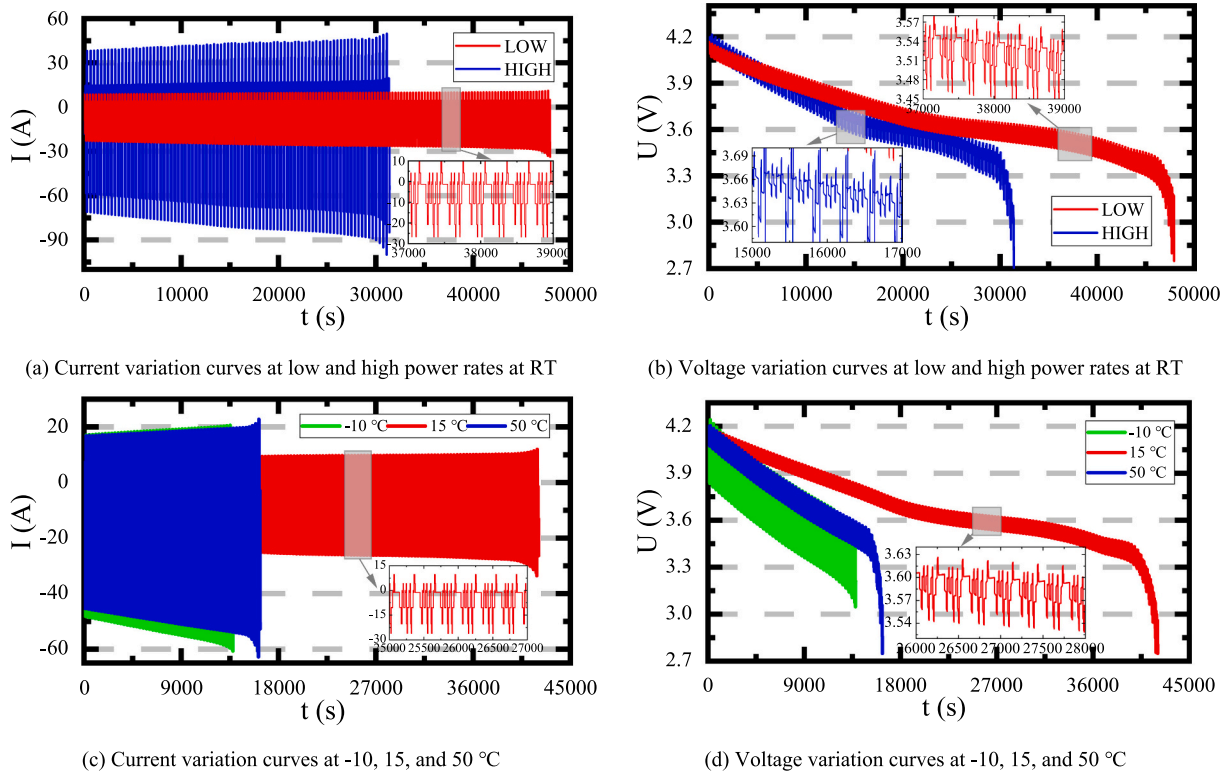| Parameter		Li-NCM70Ah	NASA #5/#6
Nominal capacity		70 Ah	1.86/2.04 Ah
Nominal voltage		3.7 V	3.7 V
Charging	Cutoff voltage	4.2 V	4.2 V
	Standard current	70 A	1.50 A
Discharging	Cutoff voltage	2.75 ± 0.05 V	2.7/2.5 V
	Standard current	3C	1C
Battery chemistry		Li-NCM	Li-NCA

A NEWARE (CT-4016-5V100A-NTFA) battery test equipment with a ±0.1% full-scale accuracy is used for the charge-discharge rate and temperature tests. It has a current range of 0.5–100 A, a range of charge- discharge voltage of 0.025–5 V, and a maximum charge-discharge power of 14 kW. A Dongguan Huitai (HT-LI-80) temperature test chamber is used to keep the battery at the defined temperature values. The results of the different test cycles and conditions considered in this paper are displayed and retrieved in real-time from the host computer connected to the NEWARE test battery system.

The different charge-discharge rate tests are carried out at RT within a temperature range of 27~32 ℃ using capacity values of 70, 35, and 21 Ah for 0.3, 0.5, and 1C, respectively, under the DST and HPPC working conditions. The BBDST is power dependent; hence, reasonable low and high-power rates are applied while ensuring the safety of the battery. For the temperature tests, after conducting three cyclic capacity tests, the average capacity values of 40, 65, and 52 Ah are obtained at −10, 15, and 50 °C, respectively. Basically, all the tests begin with the constant current-constant voltage (CC-CV) charging method, which is applied until a maximum cutoff voltage of 4.20 V is reached. Then, a 30-min rest to ensure electrochemical and thermal equilibrium is followed by the distinctive charge-discharge steps for the various working conditions until the minimum cutoff voltage is reached.

3.1.   Test procedures for the BBDST, DST, and HPPC working conditions

3.1.1 BBDST working condition tests

The experimental datasets for the BBDST working condition are obtained by processing the data retrieved from the starting, acceleration, sliding, braking, rapid acceleration, and stopping for the 19-cyclic tests for each power rate defined for the Beijing bus. Considering that charging is negative and discharging is positive, the characteristics of the current and voltage curves for the various charge-discharge power rates and temperatures are presented in Fig. 4.

(a) Current variation curves at low and high power rates at RT

(b) Voltage variation curves at low and high power rates at RT

(c) Current variation curves at -10, 15, and 50 ℃

(d) Voltage variation curves at -10, 15, and 50 ℃

Fig. 4. Characteristic current and voltage curves under the BBDST working condition.

3.1.2. DST working condition tests

The complex DST working condition is self-defined. Considering that charging is negative and discharging is positive, the characteristics of the current and voltage curves for different charge-discharge current rates and temperatures are presented in Fig. 5.

(a) Current variation curves at 0.3, 0.5, and 1 C rates at RT

(b) Voltage variation curves at 0.3, 0.5, and 1 C rates at RT

(c) Current variation curves at -10, 15, and 50 ℃

(d) Voltage variation curves at -10, 15, and 50 ℃

Fig. 5. Characteristic current and voltage curves under the DST working condition.

3.1.3. HPPC working condition tests

The HPPC test evaluates the battery's ability to pulse at various step discharge levels and time intervals. Considering that charging is negative and discharging is positive, the characteristics of the current and voltage curves for different charge-discharge current rates and temperatures are presented in Fig. 6.
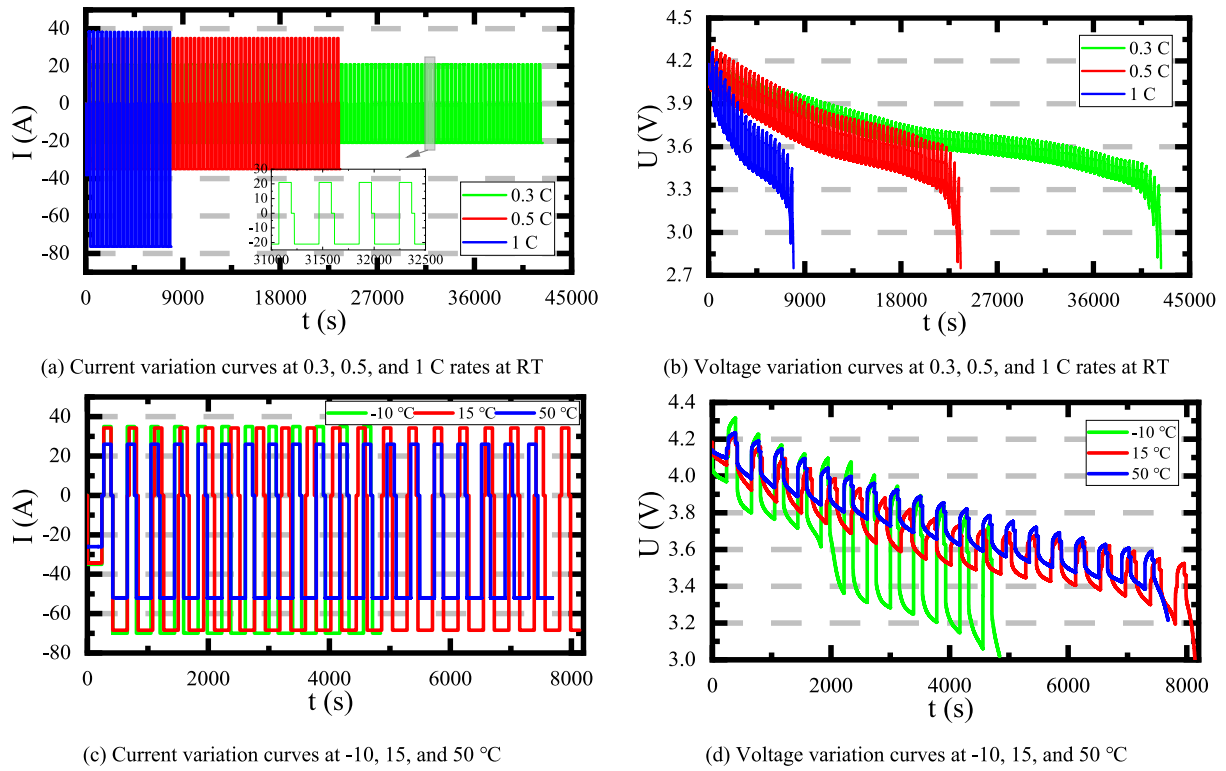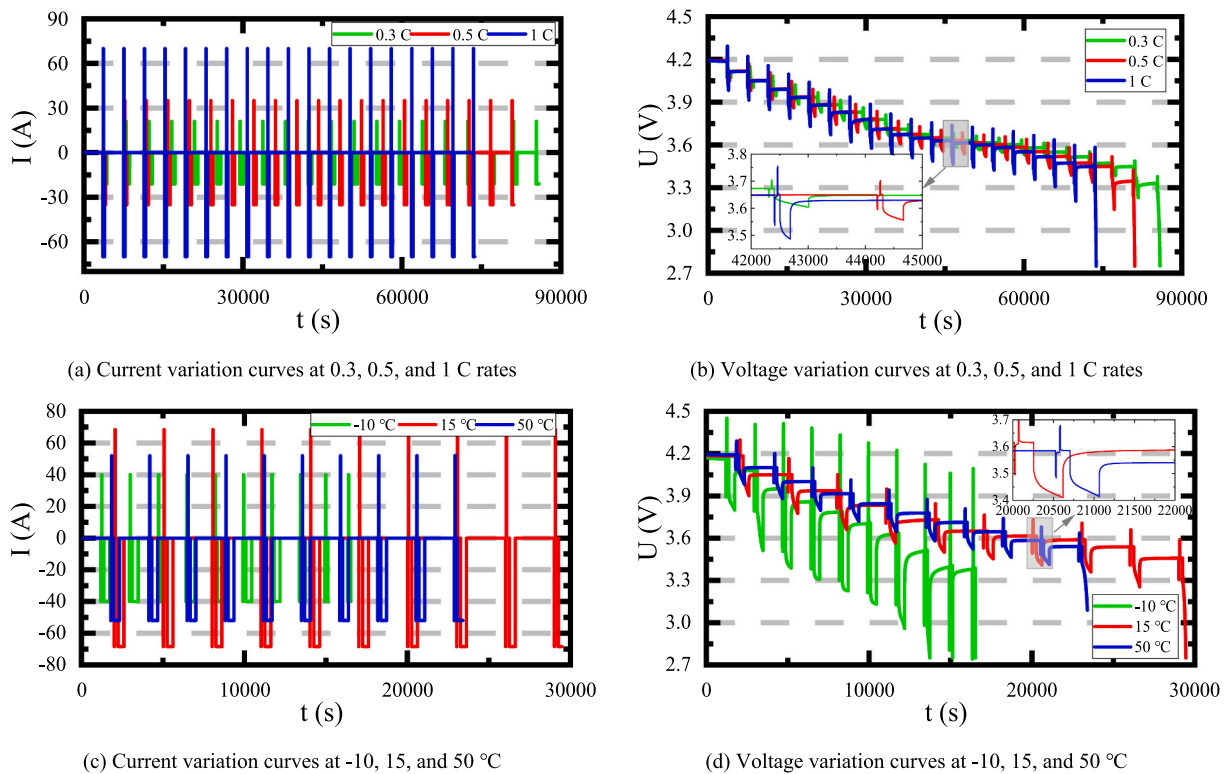

(a) Current variation curves at 0.3, 0.5, and 1 C rates

(b) Voltage variation curves at 0.3, 0.5, and 1 C rates

(c) Current variation curves at -10, 15, and 50 ℃

(d) Voltage variation curves at -10, 15, and 50 ℃

Fig. 6. Characteristic current and voltage curves under the HPPC working condition.

4. Results and discussion

The charge-discharge rate, temperature, and aging datasets are used interchangeably for training to examine the generalization and DTL abilities of the NARX and DFFNN in testing the SOC of the battery, as shown in Table 3.
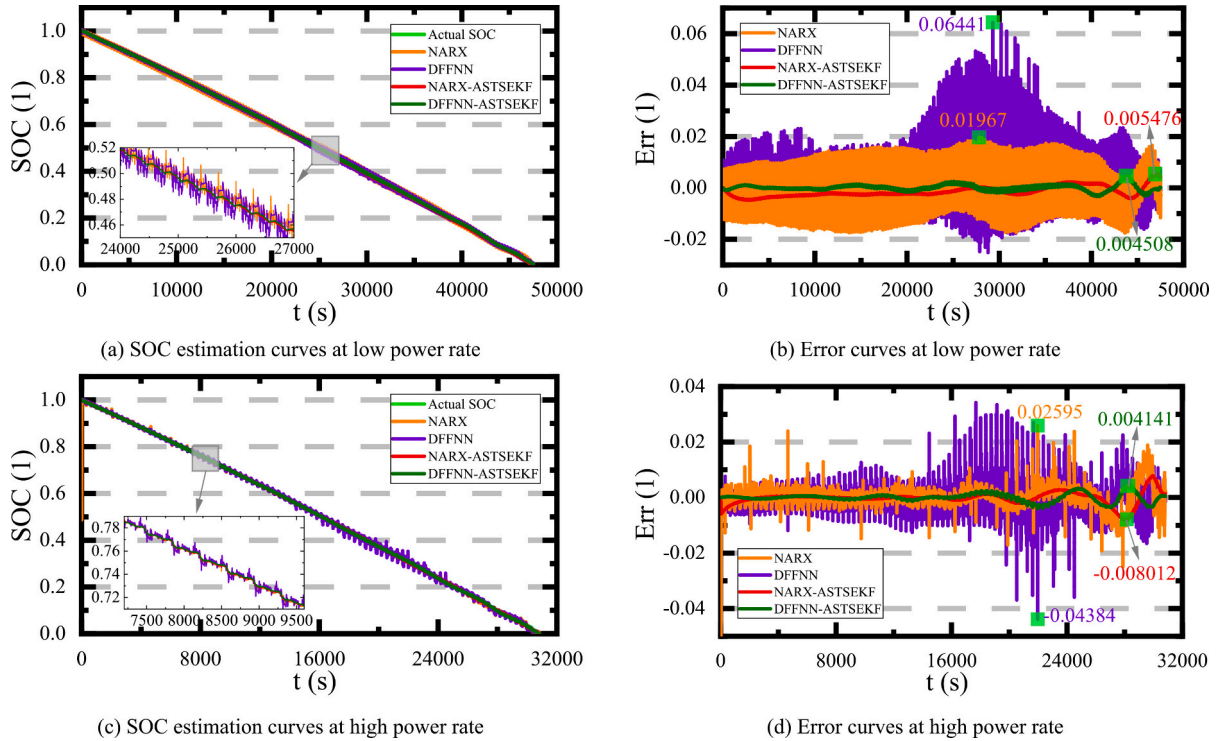
Table 3
The sequence for the training and testing of the networks.

Training conditions	Training data characteristics	Unseen testing conditions	Testing data characteristics
DST	1 C	BBDST/HPPC	0.3/0.5/1 C & −10/15/50 °C
BBDST	High power rate	DST/Battery #5/ #6	0.3/0.5/1 C & −10/15/50 °C SOH = 100/85/ 70%

Table 3 shows the sequence for the various training and testing of the networks. The training and unseen testing datasets are used logically to examine the deep learning, generalization, and DTL abilities of the networks. Specifically, all the training datasets are selected based on their low number of sampling points to reduce the computational cost while ensuring accurate testing results.

4.1. SOC estimation at different charge-discharge rates and working conditions

This section examines the SOC performance of the proposed method at various charge-discharge rates under BBDST, DST, and HPPC working conditions. The study investigates how different rates affect the SOC of the lithium-ion battery. Furthermore, the performance of data-driven networks is compared to their optimized variants based on the proposed ASTSEKF-based optimizer using the same parameter values.

(a) SOC estimation curves at low power rate

(b) Error curves at low power rate

(c) SOC estimation curves at high power rate

(d) Error curves at high power rate

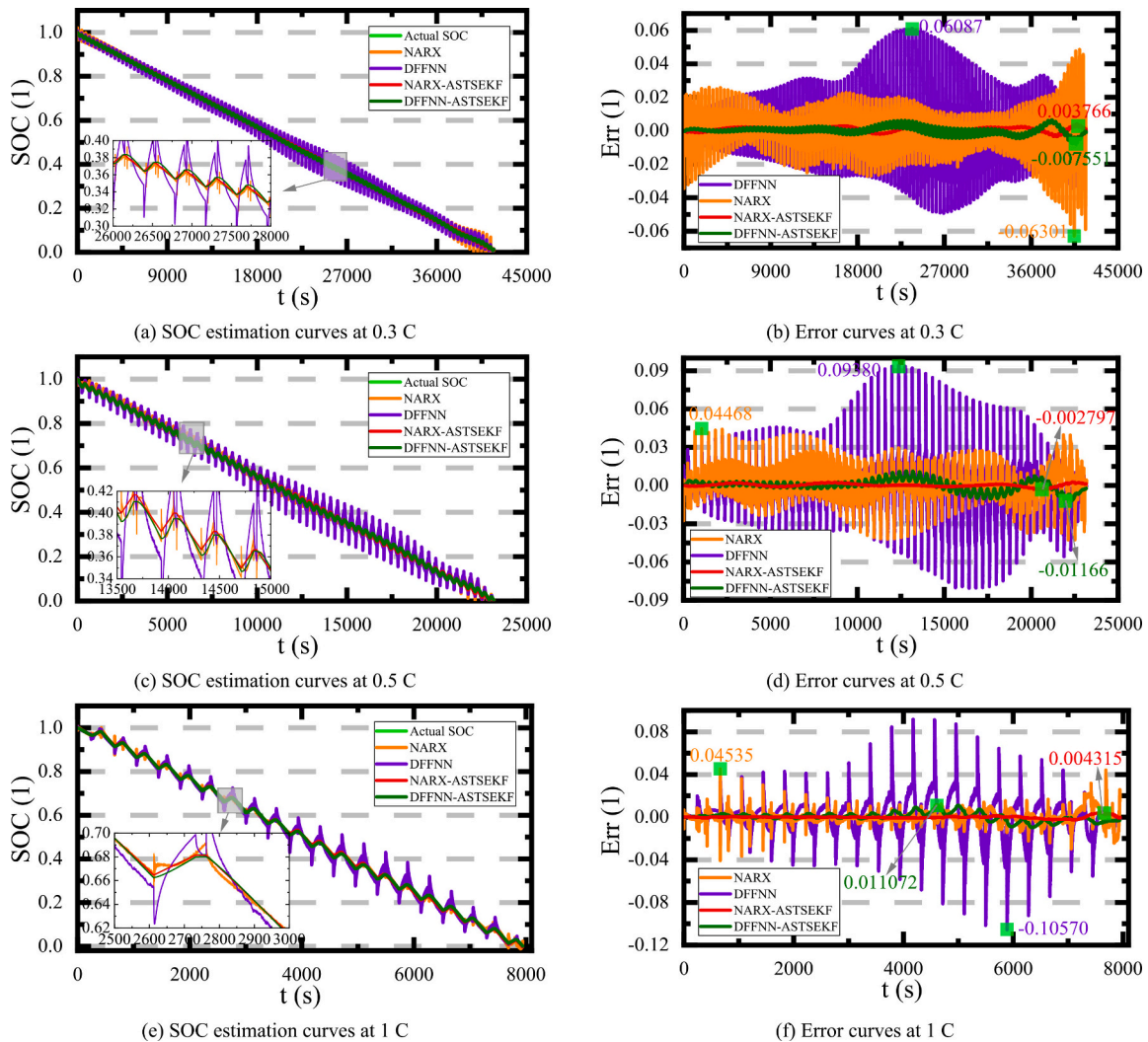**Fig. 7.** SOC estimation results of the models at different power rates under the BBDST working condition.

4.1.1. SOC estimation at different charge-discharge rates

Fig. 7 illustrates the SOC estimation outcomes of the data-driven networks and their optimized variants using the ASTSEKF method, at varying power rates of charge-discharge, while working under the BBDST working condition.

In order to understand how different power rates affect the estimation of the SOC for lithium-ion batteries, experiments are conducted at low and high-power rates under the BBDST working condition. The accuracy of the SOC is then assessed using the established networks. Then, to enhance the precision of the final SOC, the ASTSEKF method is employed to denoise, stabilize the estimates, and optimize the results.

When comparing the estimations of the NARX and DFFNN in Fig. 7, it is evident that the NARX network has less noise compared to the DFFNN, which has high and concentrated noise "spikes" at a low power rate. However, the noise of both networks at a low power rate is persistent and concentrated, while sparse-like noise is observed at a high-power rate. In Fig. 7(b) and (d), the results show that the NARX network outperforms the DFFNN in SOC estimation at both low and high-power rates. Meanwhile, the proposed ASTSEKF method effectively improves the accuracy of SOC estimation by reducing noise and optimizing the final SOC of both networks. The AME values of the NARX-ASTSEKF model are recorded as 0.5476% and 0.8012% at low and high-power rates, respectively. For the DFFNN-ASTSEKF model, the results show AME values of 0.4508% and 0.4141%, respectively. These results indicate that the ASTSEKF method is effective in denoising, maintaining stability, and enhancing the final SOC. The NARX-ASTSEKF achieved a performance improvement of 71.55% at low power rates and 69.13% at high power rates, while the DFFNN-ASTSEKF achieved an optimal improvement of 93.00% and 90.55%, respectively.

Additionally, the SOC estimation outcomes of the data-driven networks and their optimized variants utilizing the proposed ASTSEKF method at charge-discharge rates of 0.3, 0.5, and 1C under the DST working condition are displayed in Fig. 8.

(a) SOC estimation curves at 0.3 C

(b) Error curves at 0.3 C

(c) SOC estimation curves at 0.5 C

(d) Error curves at 0.5 C

(e) SOC estimation curves at 1 C

(f) Error curves at 1 C

Fig. 8. SOC estimation results of the models at different current rates under the DST working condition.

Looking at Fig. 8, it can be observed that the SOC estimated by the NARX and DFFNN models has some noisy spikes at 1 C, which is more noticeable compared to 0.5 and 0.3 C. This means that the concentration of noise around the mean decreases as the charge-discharge rate increases. When comparing the NARX and DFFNN at 0.5 and 1 C-rates, the error results indicate that the NARX has AME values of 4.468% and 4.535%, while the DFFNN, on the other hand, has AME values of 9.38% and 10.57% at the same rates, as shown in Fig. 8(d) and (f). However, at the 0.3C-rate, the NARX estimation has streamlined noise effects until about 15% SOC, which shows a high end-of-discharge noise, resulting in an AME value of 6.301%, as shown in subfigure (b). Meanwhile, the error results of the DFFNN show a similar pattern for the different cur- rent rates. On the other hand, the ASTSEKF method proposed in the study is observed to be effective in denoising, stabilizing, and optimizing the SOC of the NARX network. The proposed method resulted in low AME values of 0.3766%, 0.2797%, and 0.4315% at 0.3, 0.5, and 1 C, respectively. Additionally, the method improved the estimations of the DFFNN model, resulting in AME values of 0.7551%, 1.166%, and 1.1072%, respectively. These results suggest that the proposed method is a promising approach for optimizing battery performance.

Fig. 9 displays the SOC estimation outcomes of the data-driven networks and their optimized ASTSEKF models. These outcomes are acquired under the HPPC working condition at charge-discharge current rates of 0.3, 0.5, and 1 C.
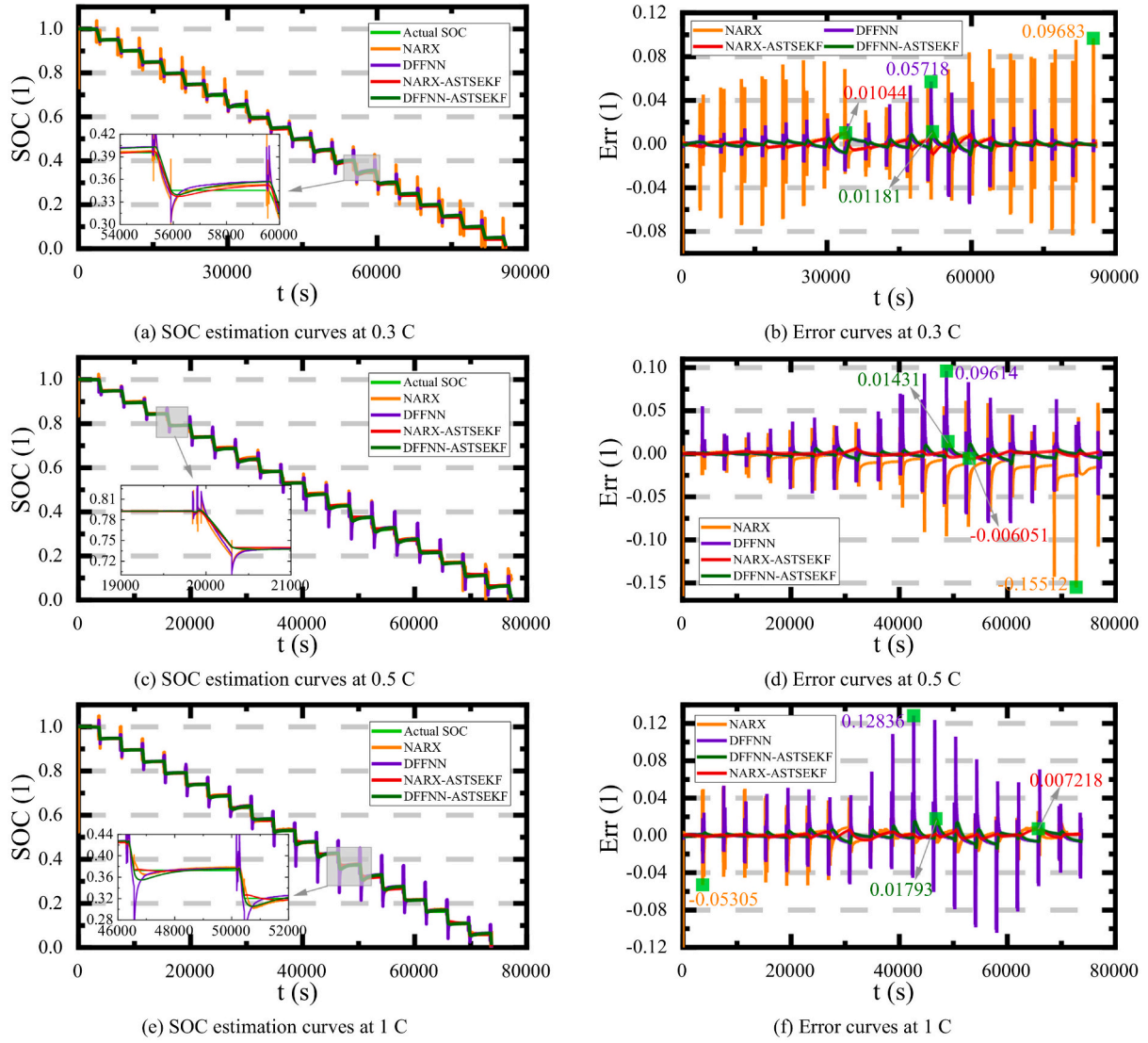
(a) SOC estimation curves at 0.3 C

(b) Error curves at 0.3 C

(c) SOC estimation curves at 0.5 C

(d) Error curves at 0.5 C

(e) SOC estimation curves at 1 C

(f) Error curves at 1 C

Fig. 9. SOC estimation results of the models at different current rates under the HPPC working condition.

When examining Fig. 9, it becomes evident that the NARX network produces more accurate results with less noise at a 1 C-rate compared to 0.3 and 0.5 C-rates (as shown in subfigures (b) and (d), respectively). On the other hand, the DFFNN's results indicate that higher current rates result in increased error and noise. However, upon observation, it is apparent that both networks have estimations with significant amounts of noise, leading to relatively high AME values. The NARX network has an AME value of 15.512%, while the DFFNN has an AME value of 12.836%. The ASTSEKF method is highly effective in enhancing the accuracy of estimating the SOC of the NARX. With AME values of 1.044%, 0.6051%, and 0.7218% at 0.3, 0.5, and 1 C rates, the method works to denoise, stabilize, and optimize the final SOC. The DFFNN-ASTSEKF model also yields good results, with AME values of 1.181%, 1.431%, and 1.793%, respectively. The proposed ASTSEKF method has proven to be effective in improving the performance of the BMS in estimating the SOC of lithium-ion batteries. At current rates of 0.3, 0.5, and 1C, it resulted in overall performance improvement of 89.22%, 96.12%, and 86.61%, respectively, which verifies that the method is useful for denoising, stabilizing, and optimizing the final SOC, making it a valuable tool for the system.

In real-time BMS applications, the proposed ASTSEKF method is effective in providing accurate and noise-free SOC estimates. This is due to the use of Cholesky decomposition and the adaptive strong tracking filter with the adaptive fading and weight adjustment factors. The method is also adaptable to various charge-discharge rates and exhibits excellent convergence.

4.1.2. Performance evaluation at different charge-discharge rates

Fig. 10 illustrates the SOC performance evaluations at various charge-discharge rates for BBDST, DST, and HPPC using the MAE, MSE, and RMSE metrics.
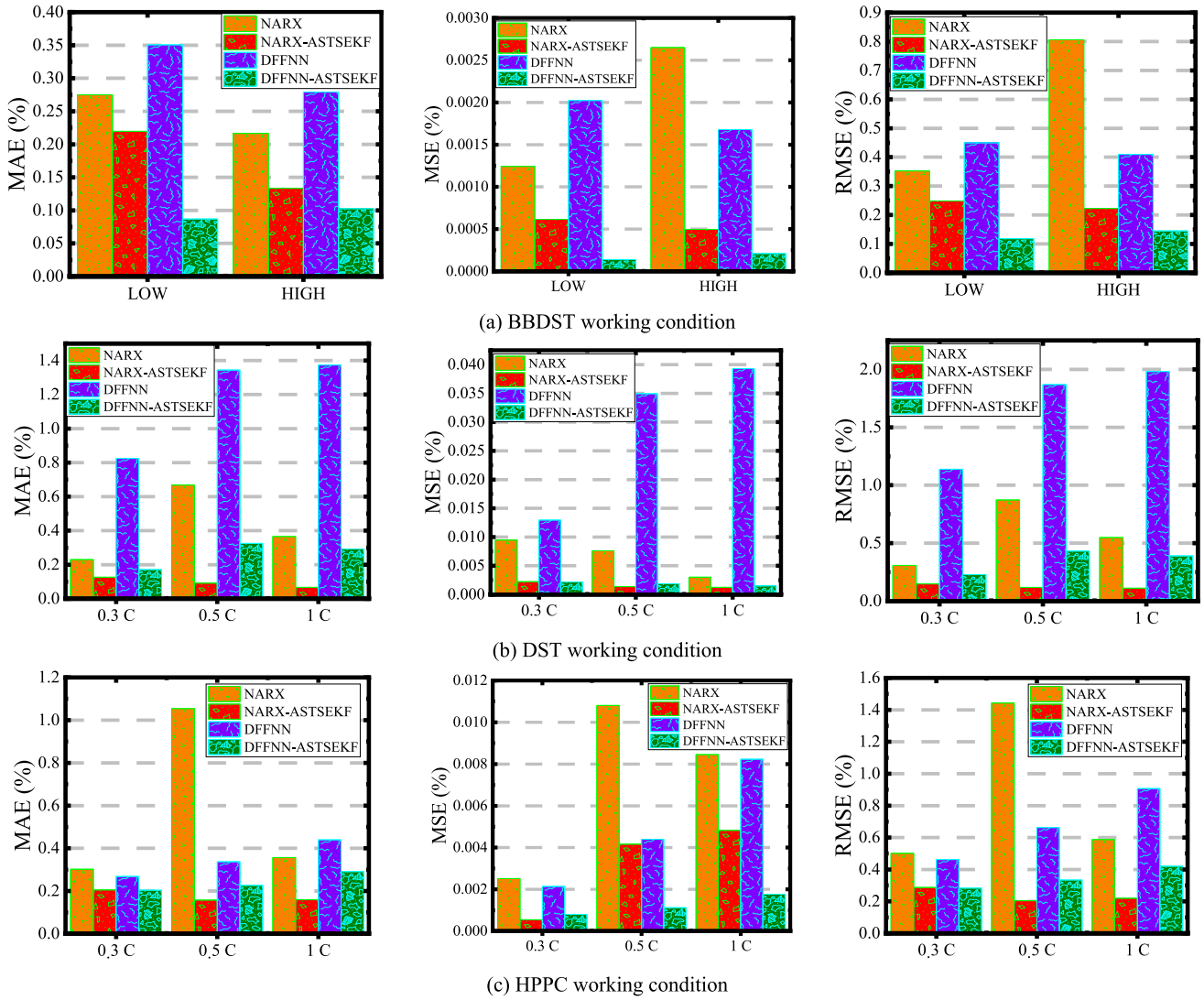
(a) BBDST working condition

(b) DST working condition

(c) HPPC working condition

Fig. 10. Performance evaluation results of the models at different charge-discharge rates.

The results of evaluating the models' performance under various working conditions, namely BBDST, DST, and HPPC, at different charge-discharge rates are shown in Fig. 10. The evaluations are based on the MAE, MSE, and RMSE metrics. Overall, the optimized models utilizing the ASTSEKF method show the most satisfactory metric values, which enhanced the performance of the corresponding networks at different charge-discharge rates and working conditions. When operating under the BBDST condition, the NARX-ASTSEKF model is the most accurate in estimating the SOC. It produces the lowest MAE, MSE, and RMSE values of 0.1334%, 0.0004958%, and 0.2227%. This represents a good improvement in the performance of 38.38%, 60.01%, and 36.82%, respectively, when compared to the NARX network. Similarly, the DFFNN-ASTSEKF model also performs well, producing the lowest MAE, MSE, and RMSE values of 0.08711%, 0.0001399%, and 0.11828%. This indicates a performance improvement of 67.53%, 91.67%, and 71.14%, respectively, when compared to the DFFNN under the same conditions. Under the DST working condition, the NARX-ASTSEKF model proves to be highly effective, with significant improvements of 70.99%, 86.86%, and 63.75% in performance compared to the NARX network. This is evidenced by having the lowest MAE, MSE, and RMSE values of 0.06516%, 0.0001243%, and 0.1115%, respectively. Similarly, the DFFNN-ASTSEKF model also demonstrated performance improvements compared to the DFFNN, with values of 0.17093%, 0.00152%, and 0.22767%, representing improvements of 79.28%, 88.28%, and 80.00%, respectively. Furthermore, under the HPPC working condition, the NARX-ASTSEKF model has shown a significant improvement in performance with the lowest MAE, MSE, and RMSE values of 0.1574%, 0.0004166%, and 0.2041%, respectively. The improvement percentages are 47.86%, 83.47%, and 59.31%. On the other hand, the DFFNN-ASTSEKF model has 0.20359%, 0.000801296%, and 0.28307%, which represent an improvement of 24.10%, 62.56%, and 61.20%, respectively.
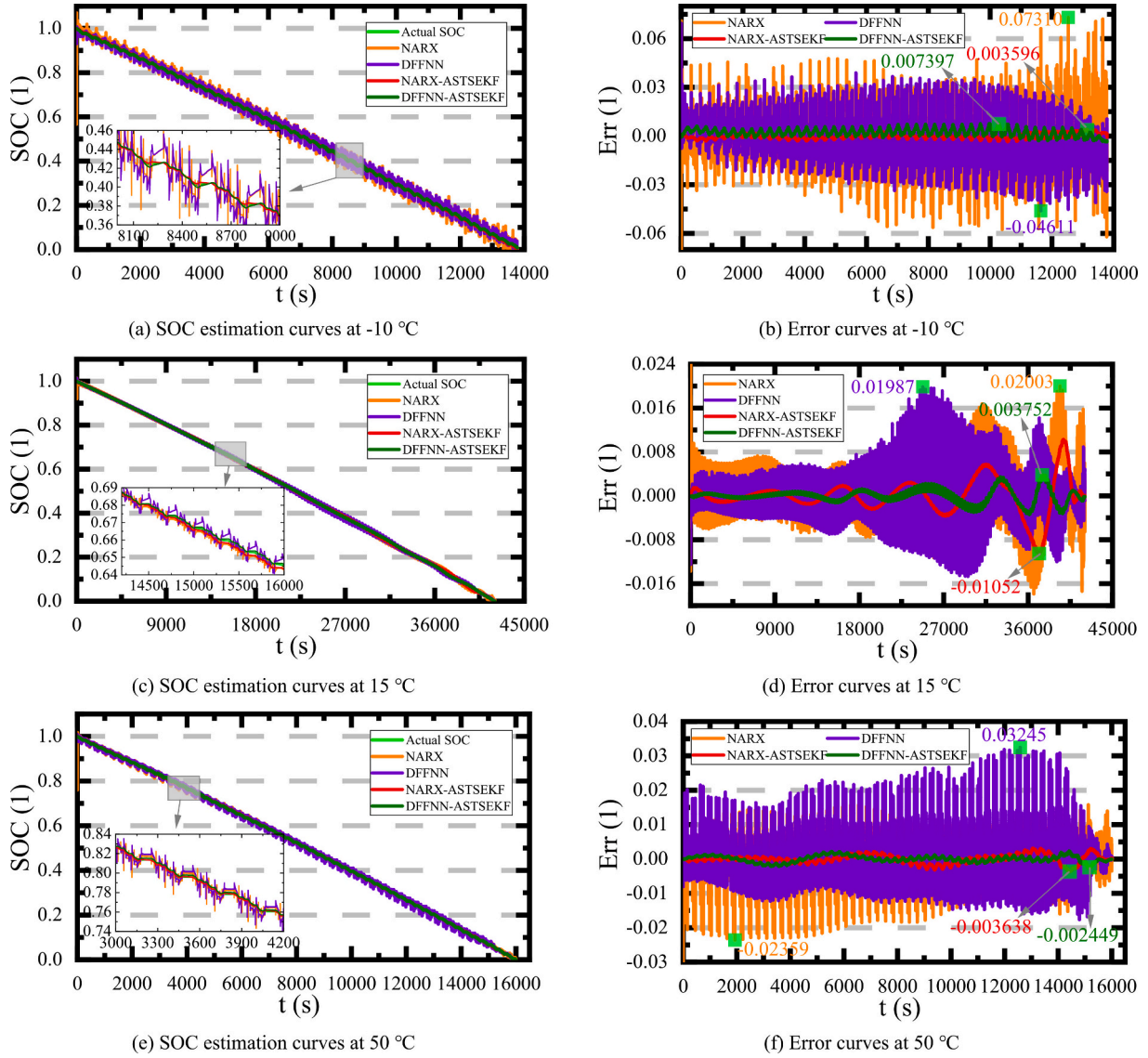
Furthermore, it is observed that the highest metric values for the NARX network occur when a current rate of 0.5 C is used for SOC estimation, especially under DST and HPPC working conditions. However, the metric error values show that the NARX network is more accurate than the DFFNN.

4.2.   SOC estimation at different operating temperatures and working conditions

In this subsection, the SOC estimations are conducted utilizing the data-driven networks and their optimized ASTSEKF models at temperatures of -10, 15, and 50 ℃ under BBDST, DST, and HPPC working conditions.

The SOC estimation results for the data-driven networks and their optimized ASTSEKF models at different temperatures under the BBDST working condition are presented in Fig. 11.

(a) SOC estimation curves at -10 ℃

(b) Error curves at -10 ℃

(c) SOC estimation curves at 15 ℃

(d) Error curves at 15 ℃

(e) SOC estimation curves at 50 ℃

(f) Error curves at 50 ℃

Fig. 11. SOC estimation results of the models at different temperatures under the BBDST working condition.

When examining Fig. 11, it becomes evident that the estimations made using NARX and DFFNN have significant levels of error and noise at a temperature of -10 ℃ in comparison to estimations made at 15 ℃ and 50 ℃. This is primarily due to the battery's high impedance and self-discharge effects, which occur during its operation in colder tempertures. When the temperature is -10 ℃, the SOC is estimated by the NARX and DFFNN to have AME values of 7.31% and 4.611%, respectively. As the temperature increases to 15 ℃, the error and noise characteristics tend to reduce, resulting in AMEs of 2.003% and 1.987% for the NARX and DFFNN, respectively, with fewer noise effects. However, as the temperature further increases to 50 ℃, the error and noise characteristics increase again, showing AME values of 2.359% and 3.245%, respectively. The ASTSEKF method has proven to be highly effective in improving the stability and optimization of the final SOC. It does this by improving the estimations of the NARX, showing AME values of 0.3596%, 1.052%, and 0.3638% at -10, 15, and 50 ℃, respectively. Additionally, the model is able to reduce noise levels during the estimation process. The DFFNN-ASTSEKF model also achieves AME values of 0.7397%, 0.3752%, and 0.2449%, respectively. The AME results indicate that the proposed ASTSEKF method significantly improves overall performance by 95.08%, 81.12%, and 92.45% at -10, 15, and 50 ℃, respectively. This method ensures a highly denoised, optimized, and steady-state final SOC estimation, achieving excellent convergence.

Fig. 12 displays the SOC estimation outcomes for the data-driven networks and their optimized ASTSEKF models, observed at temperatures of -10, 15, and 50 ℃ under the DST working condition.

(a) SOC estimation curves at -10 °C

(b) Error curves at -10 °C

(c) SOC estimation curves at 15 °C

(d) Error curves at 15 °C

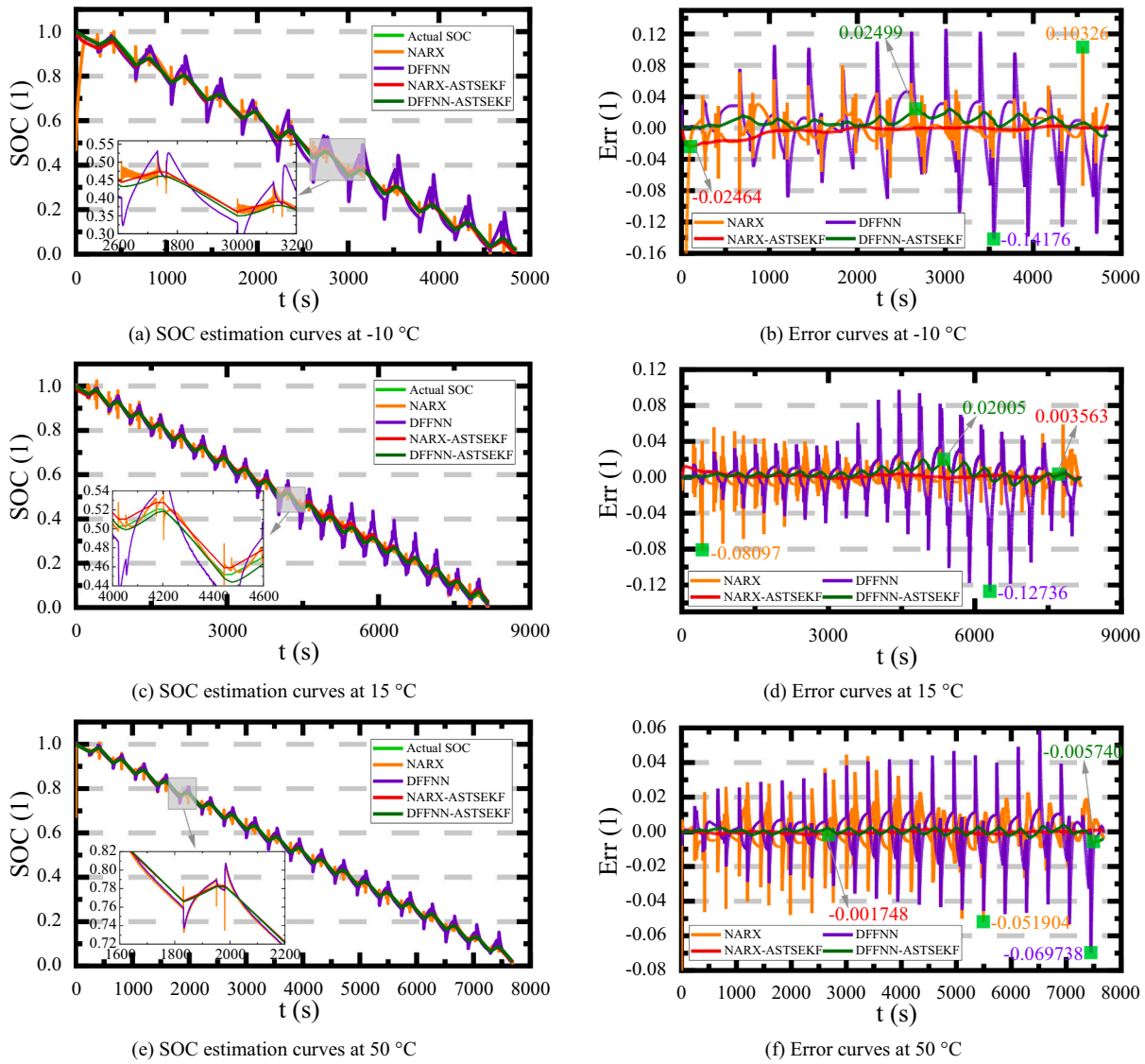(e) SOC estimation curves at 50 °C

(f) Error curves at 50 °C

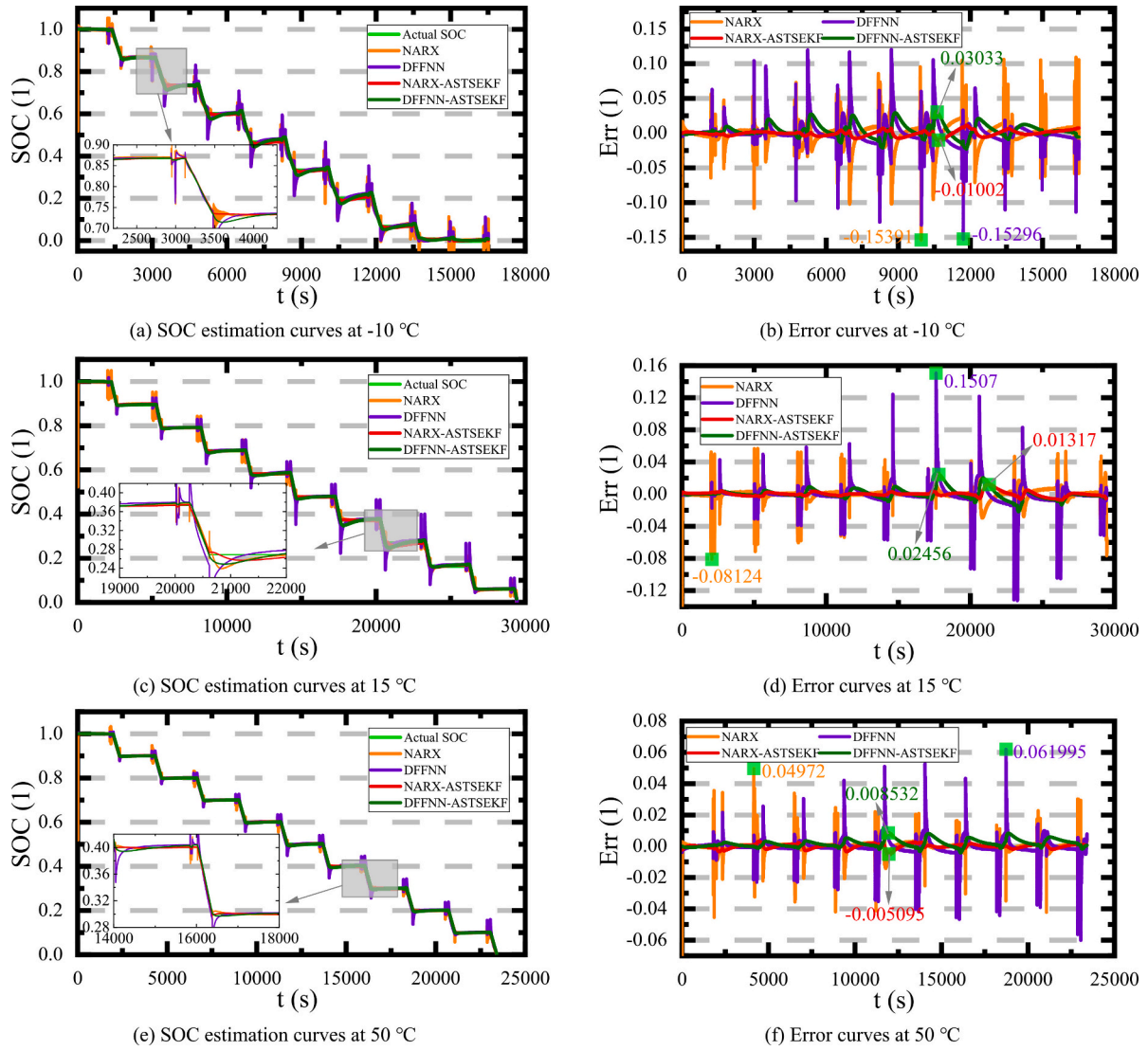**Fig. 12.** SOC estimation results of the models at different temperatures under the DST working condition.

According to Fig. 12, when compared to temperature changes of 15 and 50 ℃, the NARX and DFFNN estimations display significant noise effects at -10 ℃. These noise effects cause high error spikes, resulting in AMEs of 10.326% and 14.176%, respectively. After analyzing the data using two different methods, it can be observed that the higher the temperature, the lower the error and noise in the SOC estimations. Specifically, the NARX method produces AME values of 8.097% and 5.1904% at temperatures of 15 and 50 ℃, respectively, while the DFFNN produces AME values of 12.736% and 6.9738% at the same temperature variations. Meanwhile, the NARX-ASTSEKF model effectively denoises, stabilizes, and optimizes the final SOC with minimal errors. At -10, 15, and 50 ℃, the model achieves AME values of 2.336%, 0.3563%, and 0.1746%, respectively. The DFFNN-ASTSEKF model also performs well, with errors of 2.499%, 2.005%, and 0.5740% at the same temperature variations. According to the AME results, the proposed ASTSEKF method provides significant overall performance improvements of 82.37%, 96.25%, and 96.64% at -10, 15, and 50 ℃, respectively. This method is highly effective in optimizing the final estimation of the SOC.

Fig. 13 displays the results of SOC estimation for the data-driven networks and their ASTSEKF-based optimized models at -10, 15, and 50 ℃ under the HPPC working condition.

The estimation results in Fig. 13 show that the NARX and DFFNN estimations have a lot of noise at a temperature of -10 ℃, resulting in high error spikes, which is in contrast to the estimations at 15 and 50 ℃. At these temperatures, the NARX estimates the SOC with AME values of 15.391%, 14.883%, and 4.972%, respectively. The DFFNN also estimates the SOC with AME values of 15.296%, 15.07%, and 6.1995%, respectively, but with higher noise effects than the NARX. The results at temperatures of 15 and 50 ℃ are less noisy compared to the findings at -10 ℃, which is because the colder temperature causes high impedance and self-discharge effects. Nonetheless, the NARX-ASTSEKF model successfully smoothed and optimized the final SOC, resulting in AME values of 1.002%, 1.317%, and 0.5095% at -10, 15, and 50 ℃, respectively. In contrast, the DFFNN-ASTSEKF model has higher AME values of 3.033%, 2.456%, and 0.8532% at the same temperatures. The proposed ASTSEKF method has been found to improve optimal performance by 93.50%, 91.15%, and 89.75% at different temperatures during HPPC working conditions. This method minimizes noise and enhances the accuracy of the final SOC while ensuring quick estimation convergence.

In general, it seems that the estimations made by networks tend to be more centered around the average value. However, the presence of strong nonlinearities can lead to a lot of noise, making these estimations unsuitable for real-time SOC estimation. On the other hand, the proposed optimization models based on the ASTSEKF method offer a more accurate and noise-free SOC estimate under different working conditions, such as BBDST, DST, and HPPC. Moreover, these models can also adapt to changes in temperature, making them ideal for real-time BMS applications.

(a) SOC estimation curves at -10 ℃

(b) Error curves at -10 ℃

(c) SOC estimation curves at 15 ℃

(d) Error curves at 15 ℃

(e) SOC estimation curves at 50 ℃

(f) Error curves at 50 ℃

Fig. 13. SOC estimation results of the models at different temperatures under the HPPC working condition.

4.2.2. Performance evaluation at different operating temperatures

The results of SOC performance evaluations are conducted at temperatures of -10, 15, and 50 ℃ using the MAE, MSE, and RMSE metrics under the BBDST, DST, and HPPC working conditions, as presented in Fig. 14.

In Fig. 14, the results of performance evaluations for different models (NARX, DFFNN, and their optimized versions using the proposed ASTSEKF method) under various temperatures and working conditions (BBDST, DST, and HPPC) are presented. The evaluations are conducted using MAE, MSE, and RMSE metrics. Moreover, it is evident that the NARX-ASTSEKF model outperforms the NARX network in terms of performance. Similarly, the DFFNN-ASTSEKF model shows better results than the DFFNN model. Based on the BBDST working conditions, the NARX-ASTSEKF model has shown significant improvements compared to the NARX network. Specifically, it has achieved the lowest MAE, MSE, and RMSE values of 0.09576%, 0.00035924%, and 0.12619%, respectively, representing an improvement of 62.95%, 75.05%, and 66.70%. Additionally, the DFFNN-ASTSEKF model has performed most satisfactorily, achieving the lowest MAE, MSE, and RMSE values of 0.07258%, 0.00043952%, and 0.0911%, respectively. This indicates a performance improvement of 76.09%, 71.83%, and 76.91%. Also, the ASTSEKF-based models perform optimally at various temperatures under the DST working condition. The NARX-ASTSEKF model has the lowest MAE, MSE, and RMSE values, which are 0.06516%, 0.00258%, and 0.07943%, respectively. This respectively represents 89.82%, 65.09%, and 90.76% improvement in performance. On the other hand, the DFFNN-ASTSEKF model has the lowest MAE, MSE, and RMSE values of 0.13626%, 0.00465%, and 0.17681%, respectively compared to the DFFNN. The optimized models are evaluated at different temperatures under the HPPC working condition, and the lowest MAE, MSE, and RMSE values are recorded. The results show that the NARX-ASTSEKF model had a 41.15%, 80.11%, and 75.42% improvement in performance, while the DFFNN-ASTSEKF model showed a 33.11%, 74.95%, and 52.59% improvement, respectively.

After analyzing the results, it is observed that both the NARX and DFFNN models have the highest metric errors at -10 ℃ under the BBDST, DST, and HPPC working conditions. This is because the battery's impedance and self-discharge are both high at this temperature. However, the proposed ASTSEKF-based optimized models showed optimal results and improved the performance of the networks under different temperatures and working conditions.
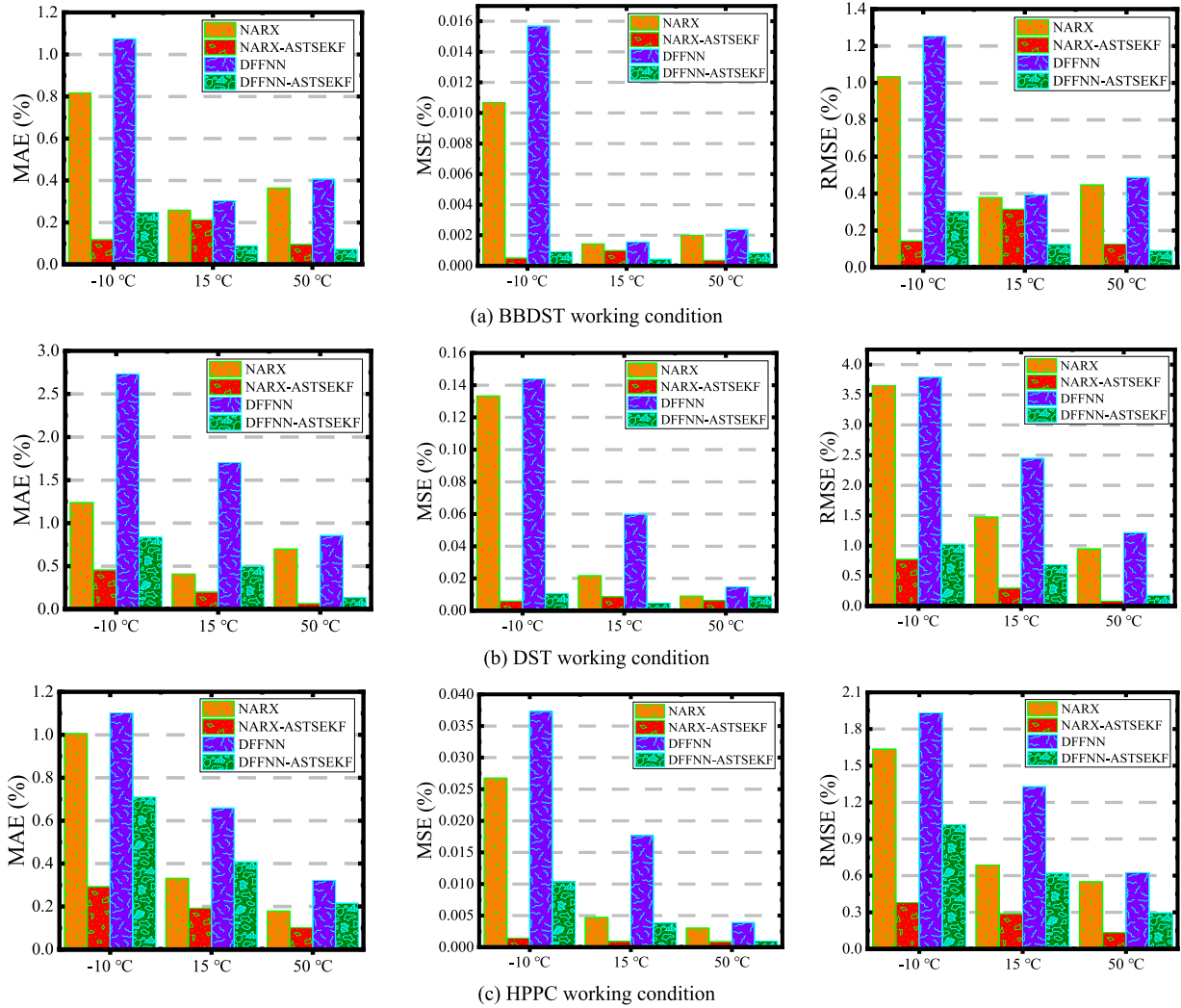
(a) BBDST working condition

(b) DST working condition

(c) HPPC working condition

Fig. 14. Performance evaluation results of the models at different temperatures.

4.3. SOC estimation at different SOH levels

The NASA Ames PCoE dataset consists of 36 lithium-ion battery datasets, which include batteries #5 and #6. Because the SOH levels extracted from the 36 batteries vary, batteries #5 and #6 are frequently used in related literature [57–59] due to their longer cycle life. At varying temperatures, they are put through three different working profiles (charge, discharge, and impedance).

Charging is conducted in a 1.5 A CC mode until the battery voltage reaches 4.2 V. Then, a CV mode is applied until the charge current is reduced to 20 mA. Discharge is carried out at a CC value of 2 A until the battery voltage drops to 2.7 V and 2.5 V for batteries #5 and #6, respectively. Electrochemical impedance spectroscopy uses frequencies ranging from 0.1 Hz to 5 kHz to measure impedance. Repeated charge-discharge cycles result in the acceleration of the battery's aging process, whereas impedance measurements provide insight into internal battery parameters that change as the battery ages. The experiments are terminated when the batteries meet the end-of-life criteria, which is a 30% fade in rated capacity (1.4 Ah) with a 70% capacity remaining for second-life applications [59]. These datasets are suitable for estimating the battery's SOC, SOH, and remaining useful life [60]. The characteristic capacity and SOH variations at different cycles for batteries #5 and #6 are presented in Fig. 15.

Using these datasets, the SOC is estimated at SOH levels of 70%, 85%, and 100% with a different number of cycles while considering the probability of the batteries being used for second-life applications. The estimations are conducted using current, voltage, capacity, and temperature datasets for each battery.
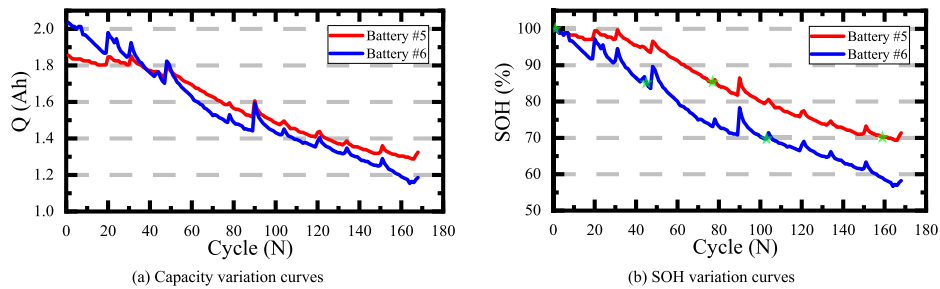

(a) Capacity variation curves

(b) SOH variation curves

Fig. 15. Capacity and SOH variation curves for batteries #5 and #6.

The SOC estimation results for the data-driven networks and their optimized ASTSEKF models at various SOH levels for battery #5 are presented in Fig. 16.
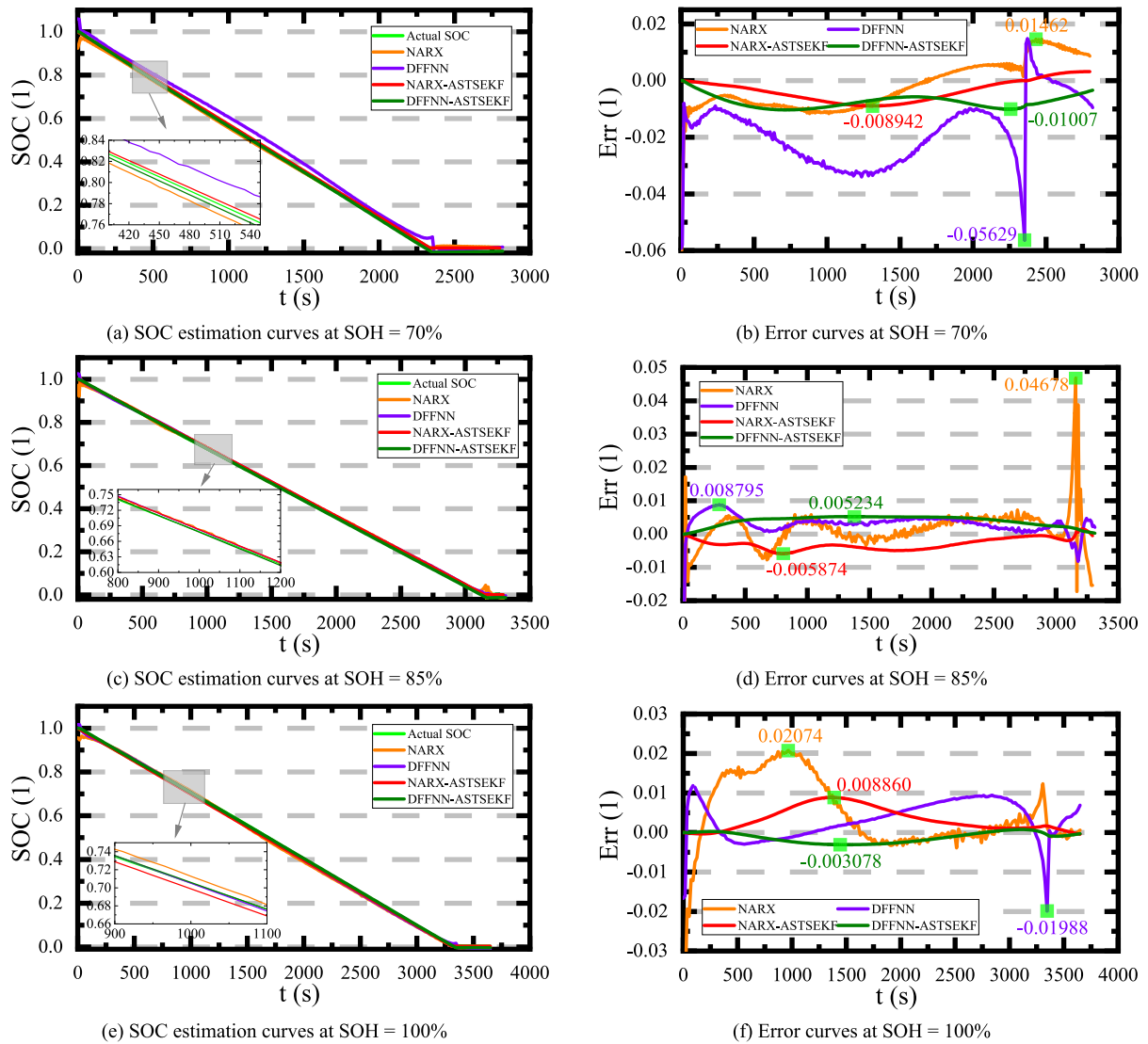

(a) SOC estimation curves at SOH = 70%   (b) Error curves at SOH = 70%

(c) SOC estimation curves at SOH = 85%   (d) Error curves at SOH = 85%

(e) SOC estimation curves at SOH = 100%   (f) Error curves at SOH = 100%

Fig. 16. SOC estimation results of the models at different SOH levels for battery **#5**.

In the provided Fig. 16, the estimation of SOC for battery #5 is carried out at varying SOH levels with the use of both NARX, DFFNN, and their ASTSEKF-optimized variants. The results indicate that the NARX network provides SOC estimates with AME values of 1.790%, 4.678%, and 2.127% at SOH levels of 70%, 85%, and 100%, respectively. At the same levels of aging, it is noticeable that the DFFNN has AME values of 5.629%, 0.8795%, and 1.988%. However, both the NARX and DFFNN show low accuracy and a suboptimal rate of convergence in estimation, with sudden fluctuations occurring at all SOH levels. Based on the results, the estimations of the NARX-ASTSEKF model are stable and well-optimized. Its results show AME values of 0.8942%, 0.5874%, and 0.8860% at SOH levels of 70%, 85%, and 100%, respectively. On the other hand, the DFFNN-ASTSEKF model has AME values of 1.007%, 0.5234%, and 0.3078%, respectively. The ASTSEKF method proposed has been found to effectively eliminate estimate fluctuations, stabilize them, and enhance the accuracy of the final SOC with rapid convergence. Furthermore, the use of AME values for both models has led to performance improvements of 82.11%, 87.44%, and 84.52% at SOH levels of 100%, 85%, and 70%, respectively.

4.3.2.   SOC estimation for battery #6

Fig. 17 displays the SOC estimation outcomes for battery #6 at varying aging stages using the data-driven networks and their optimized ASTSEKF models.
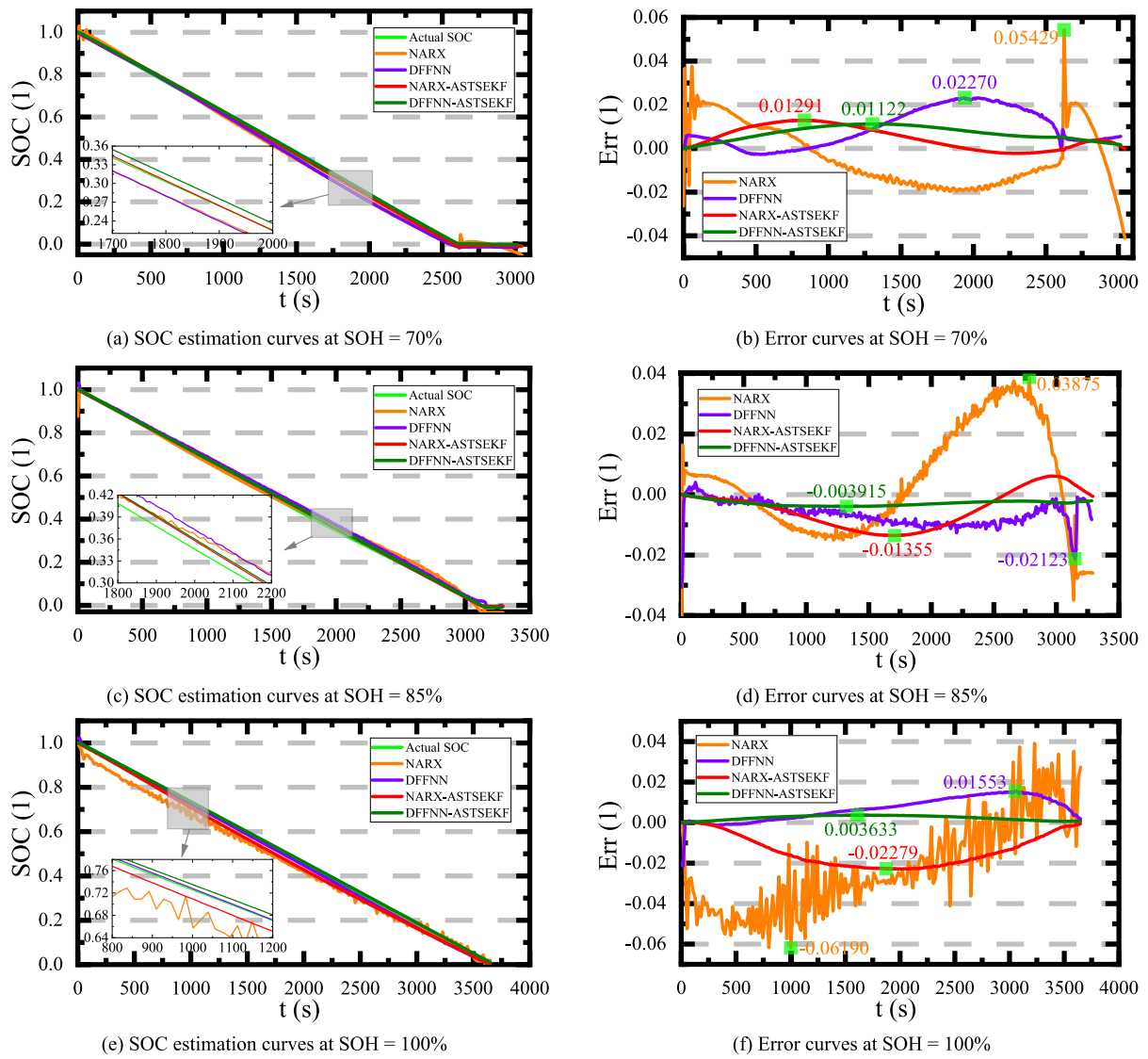
(a) SOC estimation curves at SOH = 70%

(b) Error curves at SOH = 70%

(c) SOC estimation curves at SOH = 85%

(d) Error curves at SOH = 85%

(e) SOC estimation curves at SOH = 100%

(f) Error curves at SOH = 100%

Fig. 17. SOC estimation results of the models at different SOH levels using battery **#6**.

In Fig. 17, the SOC of battery #6 is estimated at different SOH levels. The SOC estimated by the NARX network shows AME values of 5.429%, 3.875%, and 6.190% at 70%, 85%, and 100% SOH levels, respectively. On the other hand, the DFFNN showed 2.270%, 2.123%, and 1.553% at the same SOH levels. The NARX and DFFNN models both exhibit suboptimal estimation convergence with sudden changes across all SOH levels. However, the NARX-ASTSEKF model stabilizes and optimizes the estimations, resulting in AME values of 1.291%, 1.355%, and 2.279% for SOH levels of 70%, 85%, and 100%, respectively. Similarly, the DFFNN-ASTSEKF model also has AME values of 1.122%, 0.3915%, and 0.3633%, respectively. The optimized models based on ASTSEKF show minimal fluctuations and efficiently converge to optimize the final SOC accuracy. Analysis of the AME values reveals a significant performance improvement of 76.22%, 81.56%, and 76.61% at SOH levels of 70%, 85%, and 100%, respectively, when using the datasets from battery #6.

From the study, it is evident that the ASTSEKF optimization method is effective in providing reliable and consistent SOC estimates for lithium-ion batteries. This is true even for batteries with varying SOH levels and dynamic operating conditions. The results also indicate that this method can accurately estimate the SOC of second-life batteries in real-time applications.

4.3.3. Performance evaluation for batteries #5 and #6
The SOC performance evaluations using batteries #5 and #6 at different SOH levels using the MAE, MSE, and RMSE metrics are presented in Fig. 18.
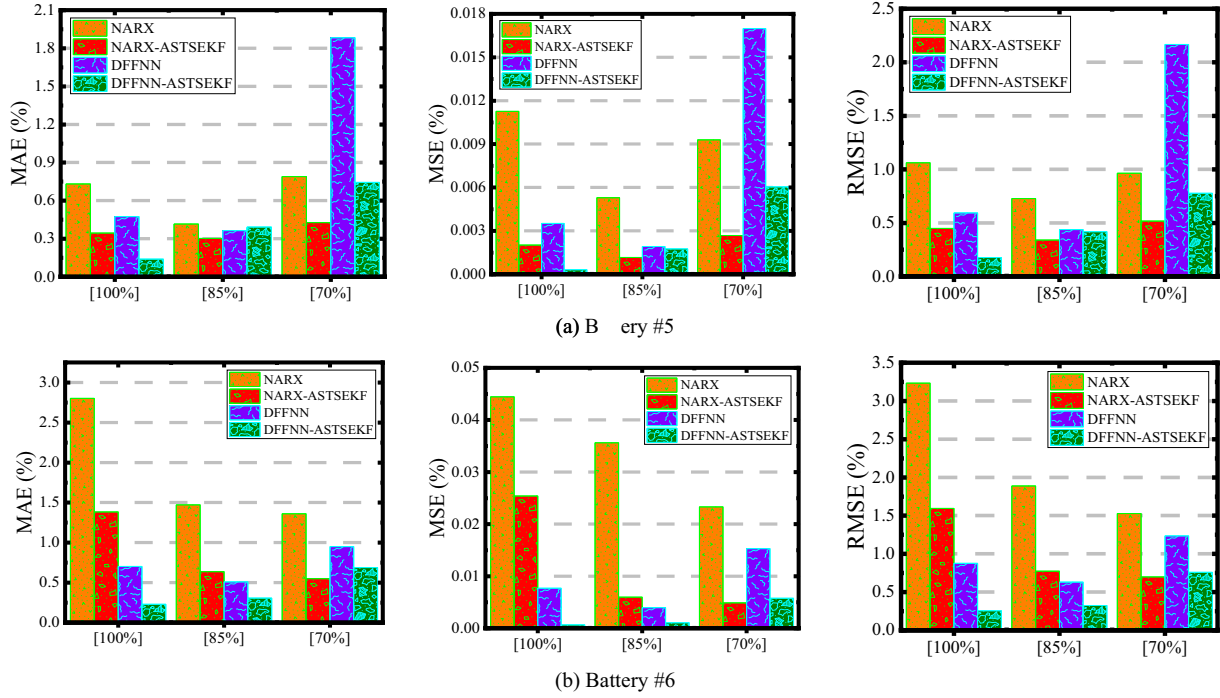
(a) Battery #5

(b) Battery #6

Fig. 18. Performance evaluation results for the NARX and NARX-ASTSEKF models at different SOH levels.

In Fig. 18, it can be observed that the performance evaluation of batteries #5 and #6 at different SOH levels using the NARX, DFFNN, and ASTSEKF-optimized models. According to the optimized models, the NARX-ASTSEKF model performs well in estimating the SOC, with the lowest MAE, MSE, and RMSE values of 0.30288%, 0.00116%, and 0.34117%, respectively. This translates to a performance improvement of 27.22%, 78.07%, and 53.08% compared to the lowest error values of the NARX using battery #5. Additionally, the DFFNN-ASTSEKF model also performs well, with 0.14034%, 0.00031567%, and 0.17767%, respectively, representing a performance improvement of 61.52%, 83.56%, and 59.48% compared to the lowest error values of the DFFNN. When battery #6 is used, the NARX-ASTSEKF model shows the lowest MAE, MSE, and RMSE values at 0.5496%, 0.00489%, and 0.6998%, respectively. This indicates a significant improvement in performance by 59.60%, 79.00 %, and 54.15%. Similarly, the DFFNN-ASTSEKF model also shows improvements in performance at various SOH levels, with values of 0.23078%, 0.00065975%, and 0.25686%. These values represent an improvement in performance by 54.79%, 82.67%, and 59.30%. These results are consistent with the test evaluations conducted on battery #5.

In general, it has been observed that the ASTSEKF-based optimized models are better suited for optimal and effective SOC estimation in real- time BMS applications. This is due to their strong tracking filter and adaptive fading and weighing factors, which provide enhanced adaptability to dynamic operating conditions, such as different charge-discharge current rates, temperatures, working conditions, and SOH levels.

4.4.   *Comparative review of the ASTSEKF-optimized models with other existing models*

To determine which SOC estimation method is superior, a comprehensive performance analysis is conducted on the ASTSEKF-based optimized models, in comparison to other existing methods. Among the methods are the GRU-AKF, affine iterative adaptive extended Kalman filter (AIAEKF), NARX-lighting search algorithm (LSA), NARX-EKF, CNN-LSTM, GRU models with transfer learning, and convolutional neural network with bidirectional weighted GRU (CNN-BWGRU) models under different verification conditions, as presented in Table 4.

Based on the evaluation results presented in Table 4, it is clear that the models optimized by the ASTSEKF are superior and more reliable compared to existing methods for estimating SOC. Among the existing methods, NARX-LSA performed well with MAE, RMSE, and MAPE values of 0.43%, 0.62%, and 3.38%, respectively, at temperatures ranging from 0 to 45 ℃ under dynamic FUDS and US06 working conditions. However, the proposed ASTSEKF-optimized models, tested and verified under various conditions, including different temperatures, charge-discharge rates, SOH levels, and dynamic BBDST, DST, and HPPC working conditions, showed optimal MAE, MSE, and RMSE values of 0.06516%, 0.0001243%, and 0.11149%, respectively.

Table 4
Comparative review of the NARX-ASTSEKF with other existing SOC estimation methods.

Method	Battery	Dynamic operating conditions	Specifications	Optimal metric values
GRU-AKF [20]	Li-FP1.1Ah	Temperatures	-10–50 °C	ME = 0.60%
		Working conditions	US06 & FUDS	RMSE = 0.20%
AIAEKF [33]	Li-NMC2Ah	Temperatures	0–45 °C	RMSE = 1.30%
		Working conditions	DST, FUDS, US06, & BJDST	
LSTM-ACKF [39]	LiFP2.2Ah	Temperatures	10–50 °C	ME = 2.2%
		Working conditions	FUDS, US06, & UDDS	RMSE = 0.8%
NARX-LSA[43]	Li-NMC2Ah	Temperatures	0–45 °C	MAE = 0.43%
		Working conditions	FUDS & US06	RMSE = 0.62%
				MAPE = 3.38%
NARX-EKF [52]	Li-NMC45Ah	Temperatures	15, 25, & 35 °C	MAE = 1.22%
		Aging cycles	42, 84, 126, & 168	RMSE = 1.41%
		Working conditions	BBDST & DST	
CNN-LSTM [61]	Li-FP1.1Ah	Temperatures	10–50 °C	MAE = 0.52%
		Working conditions	DST, FUDS, & US06	RMSE = 0.64%
GRU transfer learning [62]	Li-NCM3Ah	Temperatures	32–50 °C	ME = 4.70%
		Working conditions	FUDS, US06, &UDDS	MAE = 0.853%
				RMSE = 1.115%
CNN-BWGRU [63]	Li-NCM3Ah	Temperatures	-20–0 °C	MAE = 1.04%
		Working conditions	US06 &UDDS	RMSE = 1.37%
				R^2 = 99.76%
ASTSEKF-optimized models (Proposed)	Li-NCM70Ah & Li-NCA 1.86/2.04Ah	Temperatures	-10–50 °C	MAE = 0.06516%
		Charge-discharge rates	Low-high power rates, 1, 0.5, & 0.3C	MSE = 0.0001243%
		Aging levels	SOH = 70%, 85%, &100%	RMSE = 0.11149%
		Working conditions	BBDST, DST, & HPPC	

5. Conclusion

This paper presents an improved optimizer called ASTSEKF to denoise, stabilize, and optimize the final SOC of two deep-learning network estimations by recursive corrections. This method has enhanced dynamic operating condition adaptability, allowing for better accuracy and efficiency in battery management.

First, the NARX and DFFNN models are both constructed using DTL techniques and optimized with LM and ADAM methods to solve gradient-related issues. To overcome uncertainties in the EKF, the pro-posed ASTSEKF method uses an adaptive fading factor, a weight adjustor, and a strong tracking filter. The method also incorporates a Cholesky decomposition to recursively update the posteriori error covariance matrix.

Secondly, various experimental tests are conducted to evaluate the proposed model's performance under different working conditions for BBDST, DST, and HPPC at varying charge-discharge rates and temperatures. The effectiveness of the model is then validated using NASA datasets for batteries #5 and #6 at various aging levels. The results demonstrate that the ASTSEKF optimizer provides significant performance improvements, with maximum values of 79.28%, 91.67%, and 80.00% for MAE, MSE, and RMSE, respectively, under different charge- discharge rates and working conditions. Similarly, the model offers improvements of 89.82%, 74.95%, and 90.76% under different temperature conditions. At different aging levels, the model ensures performance improvements of 61.52%, 83.56%, and 59.48%, respectively.

Finally, in comparison with other existing methods, the performance of the proposed ASTSEKF-optimized models is superior and optimal for real-time BMS applications in EVs and batteries with different chemistries and capacities at various charge-discharge rates, operating temperatures, SOH levels, and working conditions. Furthermore, the method's formulation allows for a hybrid estimation framework without requiring an accurate and effective ECM or an OCV-SOC relationship mapping, regardless of the working conditions.

Our future work will focus on further reducing the estimation time and using the proposed ASTSEKF optimization method to enhance the performance of other methods in estimating other state parameters, such as SOH and the state of energy of lithium-ion batteries.

CRediT authorship contribution statement

Paul Takyi-Aninakwa: Methodology, conceptualization, software, writing-original draft, analysis, and data curation; **Shunli Wang**: Supervision and resources; **Hongying Zhang**: Resources and investigation; **Huan Li**: Software and writing; **Xiao Yang:** Writing; **Carlos Fernandez**: Writing.

Declaration of competing interest

The authors declare that they have no known competing financial interests or personal relationships that could have appeared to influence the work reported in this paper.

Data availability

The authors do not have permission to share data.

Acknowledgments

References

[1] M. Hossain, M.E. Haque, M.T. Arif, Kalman filtering techniques for the online model parameters and state of charge estimation of the Li-ion batteries: acomparative analysis, J. Energy Storage 51 (2022), 104174, https://doi.org/ 10.1016/j.est.2022.104174.

[2] Y. Wang, J. Tian, Z. Sun, L. Wang, R. Xu, M. Li, Z. Chen, A comprehensive review of battery modeling and state estimation approaches for advanced battery management systems, Renew. Sust. Energ. Rev. 131 (2020), 110015, https://doi. org/10.1016/j.rser.2020.110015.

[3] J. Keilz, A. Jossen, Electrochemical modeling of linear and nonlinear aging of lithium-ion cells, J. Electrochem. Soc. 167 (2020), 110535, https://doi.org/ 10.1149/1945-7111/aba44f.

[4] N.I. Shchurov, S.I. Dedov, B.V. Malozyomov, A.A. Shtang, N.V. Martyushev, R. V. Klyuev, S.N. Andriashin, Degradation of lithium-ion batteries in an electric transport complex, Energies 14 (2021) 8072, https://doi.org/10.3390/ en14238072.

[5] J.P. Fath, D. Dragicevic, L. Bittel, A. Nuhic, J. Sieg, S. Hahn, L. Alsheimer, B. Spier, T. Wetzel, Quantification of aging mechanisms and inhomogeneity in cycled lithium-ion cells by differential voltage analysis, J. Energy Storage 25 (2019), 100813, https://doi.org/10.1016/j.est.2019.100813.

[6] S. Jiang, Z. Song, Estimating the state of health of lithium-ion batteries with a high discharge rate through impedance, Energies 14 (2021) 4833, https://doi.org/ 10.3390/en14164833.

[7] L. Hu, Q. Tian, C. Zou, J. Huang, Y. Ye, X. Wu, A study on energy distribution strategy of electric vehicle hybrid energy storage system considering driving style based on real urban driving data, Renew. Sust. Energ. Rev. 162 (2022), 112416, https://doi.org/10.1016/j.rser.2022.112416.

[8] J.H. Park, J.H. Lee, S.J. Kim, I.S. Lee, Real-time state of charge estimation for each cell of lithium battery pack using neural networks, Appl. Sci. 10 (2020) 8644, https://doi.org/10.3390/app10238644.

[9] P. Takyi-Aninakwa, S. Wang, H. Zhang, X. Yang, C. Fernandez, A hybrid probabilistic correction model for the state of charge estimation of lithium-ion batteries considering dynamic currents and temperatures, Energy 273 (2023), 127231, https://doi.org/10.1016/j.energy.2023.127231.

[10] K. Yang, Y. Tang, Z. Zhang, Parameter identification and state of charge estimation for lithium-ion batteries using separated time scales and extended Kalman filter, Energies 14 (2021) 1054, https://doi.org/10.3390/en14041054.

[11] P. Takyi-Aninakwa, S. Wang, H. Zhang, Y. Xiao, C. Fernandez, Enhanced multi- state estimation methods for lithium-ion batteries considering temperature uncertainties, J. Energy Storage 66 (2023), 107495, https://doi.org/10.1016/j. est.2023.107495.

[12] D. Shin, B. Yoon, S. Yoo, Compensation method for estimating the state of charge of Li-polymer batteries using multiple long short-term memory networks based on the extended Kalman filter, Energies 14 (1–19) (2021) 349, https://doi.org/10.3390/ en14020349.

[13] P. Takyi-Aninakwa, S. Wang, H. Zhang, Y. Xiao, C. Fernandez, A NARX network optimized with an adaptive weighted square-root cubature Kalman filter for the dynamic state of charge estimation of lithium-ion batteries, J. Energy Storage 68 (2023), 107728, https://doi.org/10.1016/j.est.2023.107728.

[14] W. Duan, C. Song, S. Peng, F. Xiao, Y. Shao, S. Song, An improved gated recurrent unit network model for state-of-charge estimation of lithium-ion battery, Energies 13 (2020) 6366, https://doi.org/10.3390/en13236366.

[15] S. Wang, P. Takyi-Aninakwa, Y. Fan, C. Yu, S. Jin, C. Fernandez, D.-I. Stroe, A novel feedback correction-adaptive Kalman filtering method for the whole-life-cycle state of charge and closed-circuit voltage prediction of lithium-ion batteries based on the second-order electrical equivalent circuit model, Electr. Power Energy Syst. 139 (2022), 108020, https://doi.org/10.1016/j.ijepes.2022.108020.

[16] K. McCarthy, H. Gullapalli, K.M. Ryan, T. Kennedy, Electrochemical impedance correlation analysis for the estimation of Li-ion battery state of charge, state of health and internal temperature, J. Energy Storage 50 (2022), 104608, https://doi. org/10.1016/j.est.2022.104608.

[17] X. Xin, S.L. Wang, C. Fernandez, C.M. Yu, C.Y. Zou, J. Cong, A novel practical state of charge estimation method: an adaptive improved ampere-hour method based on composite correction factor, Int. J. Energy Res. 44 (2020), https://doi.org/10.1002/er.5758.

[18] M. Esser, G. Rohde, C. Rehtanz, Electrochemical impedance spectroscopy setup based on standard measurement equipment, J. Power Sources 544 (2022), 231869, https://doi.org/10.1016/j.jpowsour.2022.231869.

[19] J. Chen, Y. Zhang, W. Li, W. Cheng, Q. Zhu, State of charge estimation for lithium- ion batteries using gated recurrent unit recurrent neural network and adaptive Kalman filter, J. Energy Storage 55 (2022), 105396, https://doi.org/10.1016/j. est.2022.105396.

[20] H. Shi, S. Wang, J. Liang, P. Takyi-Aninakwa, X. Yang, C. Fernandez, L. Wang, Multi-time scale identification of key kinetic processes for lithium-ion batteries considering variable characteristic frequency, J. Energy Chem. 82 (2023) 521–536, https://doi.org/10.1016/j.jechem.2023.02.022.

[21] S. Leonori, L. Baldini, A. Rizzi, F.M.F. Mascioli, A physically inspired equivalent neural network circuit model for SOC estimation of electrochemical cells, Energies 14 (2021) 7386, https://doi.org/10.3390/en14217386.

[22] S. Wang, P. Ren, P. Takyi-Aninakwa, S. Jin, C. Fernandez, A critical review of improved deep convolutional neural network for multi-timescale state prediction of lithium-ion batteries, Energies 15 (2022) 5053, https://doi.org/10.3390/ en15145053.

[23] Y. Song, D. Liu, H. Liao, Y. Peng, A hybrid statistical data-driven method for on-line joint state estimation of lithium-ion batteries, Appl. Energy 261 (2020), 114408, https://doi.org/10.1016/j.apenergy.2019.114408.

[24] P. Takyi-Aninakwa, S. Wang, H. Zhang, E. Appiah, E.D. Bobobee, C. Fernandez, A strong tracking adaptive fading-extended Kalman filter for the state of charge estimation of lithium-ion batteries, Int. J. Energy Res. 46 (2022), https://doi.org/ 10.1002/er.8307.

[25] Y. Zhang, T. Wik, J. Bergstro¨m, M. Pecht, C. Zou, A machine learning-based framework for online prediction of battery ageing trajectory and lifetime using histogram data, J. Power Sources 526 (2022), 231110, https://doi.org/10.1016/j. jpowsour.2022.231110.

[26] S. Luciani, S. Feraco, A. Bonfitto, A. Tonoli, Hardware-in-the-loop assessment of a data-driven state of charge estimation method for lithium-ion batteries in hybrid vehicles, Electronics 10 (2021) 2828, https://doi.org/10.3390/ electronics10222828.

[27] Y. Wang, Z. Chen, A framework for state-of-charge and remaining discharge time prediction using unscented particle filter, Appl. Energy 260 (2020), 114324, https://doi.org/10.1016/j.apenergy.2019.114324.

[28] M. Ragone, V. Yurkiv, A. Ramasubramanian, B. Kashir, F. Mashayek, Data driven estimation of electric vehicle battery state-of-charge informed by automotive simulations and multi-physics modeling, J. Power Sources 483 (2021), 229108, https://doi.org/10.1016/j.jpowsour.2020.229108.

[29] Z. Cui, C. Wang, X. Gao, S. Tian, State of health estimation for lithium-ion battery based on the coupling-loop nonlinear autoregressive with exogenous inputs neural network, Electrochim. Acta 393 (2021), 139047, https://doi.org/10.1016/j. electacta.2021.139047.

[30] I. Oyewole, A. Chehade, Y. Kim, A controllable deep transfer learning network with multiple domain adaptation for battery state-of-charge estimation, Appl. Energy 312 (2022), 118726, https://doi.org/10.1016/j.apenergy.2022.118726.

[31] Z. Xi, R. Wang, Y. Fu, C. Mi, Accurate and reliable state of charge estimation of lithium-ion batteries using time-delayed recurrent neural networks through the identification of overexcited neurons, Appl. Energy 305 (2022), 117962, https:// doi.org/10.1016/j.apenergy.2021.117962.

[32] P. Takyi-Aninakwa, S. Wang, H. Zhang, X. Yang, C. Fernandez, An optimized long short-term memory-weighted fading extended Kalman filtering model with wide temperature adaptation for the state of charge estimation of lithium-ion batteries, Appl. Energy 326 (2022), 120043, https://doi.org/10.1016/j. apenergy.2022.120043.

[33] Q. Wang, M. Ye, M. Wei, G. Lian, Y. Li, Deep convolutional neural network based closed-loop SOC estimation for lithium-ion batteries in hierarchical scenarios, Energy 263 (2023), 125718, https://doi.org/10.1016/j.energy.2022.125718.

[34] J. Hong, Z. Wang, W. Chen, L.-Y. Wang, C. Qu, Online joint-prediction of multi- forward-step battery SOC using LSTM neural networks and multiple linear regression for real-world electric vehicles, J. Energy Storage 30 (2020), 101459, https://doi.org/10.1016/j.est.2020.101459.

[35] P. Takyi-Aninakwa, S. Wang, H. Zhang, H. Li, W. Xu, C. Fernandez, An optimized relevant long short-term memory-squared gain extended Kalman filter for the state of charge estimation of lithium-ion batteries, Energy 260 (2022), 125093, https:// doi.org/10.1016/j.energy.2022.125093.

[36] X. Fan, W. Zhang, C. Zhang, A. Chen, F. An, SOC estimation of Li-ion battery using convolutional neural network with U-Net architecture, Energy 256 (2022), 124612, https://doi.org/10.1016/j.energy.2022.124612.

[37] J. Chen, C. Lu, C. Chen, H. Cheng, D. Xuan, An improved gated recurrent unit neural network for state-of-charge estimation of lithium-ion battery, Appl. Sci. 12 (2022) 2305, https://doi.org/10.3390/app12052305.

[38] F. Yang, W. Li, C. Li, Q. Miao, State-of-charge estimation of lithium-ion batteries based on gated recurrent neural network, Energy 175 (2019) 66–75, https://doi. org/10.1016/j.energy.2019.03.059.

[39] Y. Tian, R. Lai, X. Li, L. Xiang, J. Tian, A combined method for state-of-charge estimation for lithium-ion batteries using a long short-term memory network and an adaptive cubature Kalman filter, Appl. Energy 265 (2020), 114789, https://doi. org/10.1016/j.apenergy.2020.114789.

[40] C. Bian, H. He, S. Yang, Stacked bidirectional long short-term memory networks for state-of-charge estimation of lithium-ion batteries, Energy 191 (2020), 116538, https://doi.org/10.1016/j.energy.2019.116538.

[41] Q. Wang, H. Gu, M. Ye, M. Wei, X. Xu, State of charge estimation for lithium-ion battery based on NARX recurrent neural network and moving window method, IEEE Access 9 (2021) 83364–83375, https://doi.org/10.1109/ ACCESS.2021.3086507.

[42] A. Herle, J. Channegowda, K. Naraharisetti, Analysis of NARXNN for state of charge estimation for li-ion batteries on various drive cycles, in: 2020 8th International Conference on Power Electronics Systems and Applications (PESA), 2020, pp. 1–4, https://doi.org/10.1109/PESA50370.2020.9344002.

[43] M.S. Lipu, M.A. Hannan, A. Hussain, M.H. Saad, A. Ayob, F. Blaabjerg, State of charge estimation for lithium-ion battery using recurrent NARX neural network model-based lighting search algorithm, IEEE Access 6 (2018) 28150–28161, https://doi.org/10.1109/access.2018.2837156.

[44] W. Sun, Y. Qiu, L. Sun, Q. Hua, Neural network-based learning and estimation of battery state-of-charge: a comparison study between direct and indirect methodology, Int. J. Energy Res. 44 (2020) 10307–10319, https://doi.org/ 10.1002/er.5654.

[45] C. Guo, G. Yuan, C. Zhu, X. Wang, X. Cao, SOC estimation for lithium-ion battery using recurrent NARX neural network and genetic algorithm, in: IOP Conf. Series: Materials Science and Engineering 486, IOP Publishing, 2019, p. 012076, https:// doi.org/10.1088/1757-899X/486/1/012076.

[46] G. Abbas, M. Nawaz, F. Kamran, Performance comparison of NARX & RNN-LSTM neural networks for LiFePO$_4$ battery state of charge estimation, in: 2019 16th International Bhurban Conference on Applied Sciences and Technology (IBCAST) 22, 2019, pp. 463–468, https://doi.org/10.1109/IBCAST.2019.8667172.

[47] M. Wei, M. Ye, J.B. Li, Q. Wang, X. Xu, State of charge estimation of lithium-ion batteries using LSTM and NARX neural networks, IEEE Access 8 (2020) 189236–189245, https://doi.org/10.1109/ACCESS.2020.3031340.

[48] M. Adaikkappan, N. Sathiyamoorthy, Modeling, state of charge estimation, and charging of lithium-ion battery in electric vehicle: a review, Int. J. Energy Res. 46 (2022), https://doi.org/10.1002/er.7339.

[49] B. Yang, J. Wang, P. Cao, T. Zhu, H. Shu, J. Chen, J. Zhang, J. Zhu, Classification, summarization and perspectives on state-of-charge estimation of lithium-ion batteries used in electric vehicles: a critical comprehensive survey, J. Energy Storage 39 (2021), 102572, https://doi.org/10.1016/j.est.2021.102572.

[50] J. Tian, R. Xiong, W. Shen, J. Lu, State-of-charge estimation of LiFePO4 batteries in electric vehicles: a deep-learning enabled approach, Appl. Energy 291 (2021), 116812, https://doi.org/10.1016/j.apenergy.2021.116812.

[51] J. Chen, J. Zhang, X. Xu, C. Fu, D. Zhang, Q. Zhang, Q. Xuan, E-LSTM-D: a deep learning framework for dynamic network link prediction, IEEE Trans. Syst. Man Cybern. Syst. Hum. 51 (2019) 3699–3712, https://doi.org/10.1109/ TSMC.2019.2932913.

[52] H. Li, C. Zou, C. Fernandez, S. Wang, Y. Fan, D. Liu, A novel state of charge estimation for energy storage systems based on the joint NARX network and filter algorithm, Int. J. Electrochem. Sci. 16 (2021), 211213, https://doi.org/10.20964/ 2021.12.50.

[53] Z. Deng, X. Hu, X. Lin, Y. Che, L. Xu, W. Guo, Data-driven state of charge estimation for lithium-ion battery packs based on Gaussian process regression, Energy 205 (2020), 118000, https://doi.org/10.1016/j.energy.2020.118000.

[54] B. Xia, D. Cui, Z. Sun, Z. Lao, R. Zhang, W. Wang, W. Sun, Y. Lai, M. Wang, State of charge estimation of lithium-ion batteries using optimized Levenberg-Marquardt wavelet neural network, Energy 153 (2018) 694–705, https://doi.org/10.1016/j. energy.2018.04.085.

[55] P.C. Bolsi, E.O. Prado, A.C.C. Lima, H.C. Sartori, J.R. Pinheiro, Battery autonomy estimation method applied to lead–acid batteries in uninterruptible power supplies, J. Energy Storage 58 (2023), 106421, https://doi.org/10.1016/j. est.2022.106421.

[56] L. Gong, Z. Zhang, Y. Li, X. Li, K. Sun, P. Tan, Voltage-stress-based state of charge estimation of pouch lithium-ion batteries using a long short-term memory network, J. Energy Storage 55 (2022), 105720, https://doi.org/10.1016/j.est.2022.105720.

[57] A. Bavand, S.A. Khajehoddin, M. Ardakani, A. Tabesh, Online estimations of Li-ion battery SOC and SOH applicable to partial charge/discharge, IEEE Trans. Transp. Electr. 8 (2022) 3673–3685, https://doi.org/10.1109/TTE.2022.3162164.

[58] S. Jafari, Z. Shahbazi, Y.-C. Byun, S.-J. Lee, Lithium-ion battery estimation in online framework using extreme gradient boosting machine learning approach, Mathematics 10 (2022) 888, https://doi.org/10.3390/math10060888.

[59] M.F. Bo¨rner, M.H. Frieges, B. Sp¨ath, K. Sp¨utz, H.H. Heimes, D.U. Sauer, W. Li, Challenges of second-life concepts for retired electric vehicle batteries, Cell Rep. Phys. Sci. 3 (2022), 101095, https://doi.org/10.1016/j.xcrp.2022.101095.

[60] S. Jo, S. Jung, T. Roh, Battery state-of-health estimation using machine learning and preprocessing with relative state-of-charge, Energies 14 (2021) 7206, https:// doi.org/10.3390/en14217206.

[61] X. Song, F. Yang, D. Wang, K.-L. Tsui, Combined CNN-LSTM network for state-of- charge estimation of lithium-ion batteries, IEEE Access 7 (2019) 88894–88902, https://doi.org/10.1109/ACCESS.2019.2926517.

[62] Y. Wang, Z. Chen, W. Zhang, Lithium-ion battery state-of-charge estimation for small target sample sets using the improved GRU-based transfer learning, Energy 244 (2022), 123178, https://doi.org/10.1016/j.energy.2022.123178.

[63] Z. Cui, L. Kang, L. Li, L. Wang, K. Wang, A hybrid neural network model with improved input for state of charge estimation of lithium-ion battery at low temperatures, Renew. Energy 198 (2022) 1328–1340, https://doi.org/10.1016/j. renene.2022.08.123